

THE JCMT BISTRO SURVEY: THE MAGNETIC FIELD OF THE BARNARD 1 STAR-FORMING REGION

THE B-FIELDS IN STAR-FORMING REGIONS OBSERVATIONS (BISTRO) COLLABORATION

SIMON COUDÉ,^{1,2} PIERRE BASTIEN,^{3,2} MARTIN HOUDE,⁴ SARAH SADAVOY,⁵ RACHEL FRIESSEN,⁶ JAMES DI FRANCESCO,^{7,8} DOUG JOHNSTONE,^{7,8} STEVE MAIRS,⁹ TETSUO HASEGAWA,¹⁰ WOOJIN KWON,^{11,12} SHIH-PING LAI,^{13,14} KEPING QIU,^{15,16} DEREK WARD-THOMPSON,¹⁷ DAVID BERRY,⁹ MICHAEL CHUN-YUAN CHEN,⁷ JASON FIEGE,¹⁸ ERICA FRANZMANN,¹⁸ JENNIFER HATCHELL,¹⁹ KEVIN LACAILLE,^{20,21} BRENDA C. MATTHEWS,^{7,8} GERALD H. MORIARTY-SCHIEVEN,⁸ ANDY PON,⁴ PHILIPPE ANDRÉ,²² DORIS ARZOUMANIAN,²³ YUSUKE ASO,²⁴ DO-YOUNG BYUN,^{11,12} ESWARAIH CHAKALI,¹³ HUEI-RU CHEN,^{13,14} WEN PING CHEN,²⁵ TAO-CHUNG CHING,^{13,26} JUNGYEON CHO,²⁷ MINHO CHOI,¹¹ ANTONIO CHRYSOSTOMOU,²⁸ EUN JUNG CHUNG,¹¹ YASUO DOI,²⁹ EMILY DRABEK-MAUNDER,³⁰ C. DARREN DOWELL,³¹ STEWART P. S. EYRES,³² SAM FALLE,³³ PER FRIBERG,⁹ GARY FULLER,³⁴ RAY S. FURUYA,^{35,36} TIM GLEDHILL,²⁸ SARAH F. GRAVES,⁹ JANE S. GREAVES,³⁰ MATT J. GRIFFIN,³⁰ QILAO GU,³⁷ SAEKO S. HAYASHI,³⁸ THIEM HOANG,¹¹ WAYNE HOLLAND,^{39,40} TSUYOSHI INOUE,²³ SHU-ICHIRO INUTSUKA,²³ KAZUNARI IWASAKI,⁴¹ IL-GYO JEONG,¹¹ YOSHIHIRO KANAMORI,²⁹ AKIMASA KATAOKA,⁴² JI-HYUN KANG,¹¹ MIJU KANG,¹¹ SUNG-JU KANG,¹¹ KOJI S. KAWABATA,^{43,44,45} FRANCISCA KEMPER,¹⁴ GWANJEONG KIM,^{11,12,46} JONGSOO KIM,^{11,12} KEE-TAE KIM,¹¹ KYOUNG HEE KIM,⁴⁷ MI-RYANG KIM,¹¹ SHINYOUNG KIM,^{11,12} JASON M. KIRK,³² MASATO I.N. KOBAYASHI,²³ PATRICK M. KOCH,¹⁴ JUNGMI KWON,⁴⁸ JEONG-EUN LEE,⁴⁹ CHANG WON LEE,^{11,12} SANG-SUNG LEE,^{11,12} DALEI LI,⁵⁰ DI LI,²⁶ HUA-BAI LI,³⁷ HONG-LI LIU,³⁷ JUNHAO LIU,^{15,16} SHENG-YUAN LIU,¹⁴ TIE LIU,^{11,9} SVEN VAN LOO,⁵¹ A-RAN LYU,¹¹ MASAFUMI MATSUMURA,⁵² TETSUYA NAGATA,⁵³ FUMITAKA NAKAMURA,^{42,54} HIROYUKI NAKANISHI,⁵⁵ NAGAYOSHI OHASHI,³⁸ TAKASHI ONAKA,²⁴ HARRIET PARSONS,⁹ KATE PATTLE,¹³ NICOLAS PERETTO,³⁰ TAE-SOO PYO,^{38,54} LEI QIAN,²⁶ RAMPRASAD RAO,¹⁴ MARK G. RAWLINGS,⁹ BRENDAN RETTER,³⁰ JOHN RICHER,^{56,57} ANDREW RIGBY,³⁰ JEAN-FRANÇOIS ROBITAILLE,⁵⁸ HIRO SAITO,⁵⁹ GIORGIO SAVINI,⁶⁰ ANNA M. M. SCAIFE,³⁴ MASUMICHI SETA,⁶¹ HIROKO SHINNAGA,⁵⁵ ARCHANA SOAM,^{1,11} MOTOHIDE TAMURA,²⁴ YA-WEN TANG,¹⁴ KOHJI TOMISAKA,^{42,54} YUSUKE TSUKAMOTO,⁵⁵ HONGCHI WANG,⁶² JIA-WEI WANG,¹³ ANTHONY P. WHITWORTH,³⁰ HSI-WEI YEN,^{14,63} HYUNJU YOO,²⁷ JINGHUA YUAN,²⁶ TETSUYA ZENKO,⁵³ CHUAN-PENG ZHANG,²⁶ GUOYIN ZHANG,²⁶ JIANJUN ZHOU,⁵⁰ AND LEI ZHU²⁶

¹ SOFIA Science Center, Universities Space Research Association, NASA Ames Research Center, M.S. N232-12, Moffett Field, CA 94035, USA

² Centre de Recherche en Astrophysique du Québec (CRAQ), Université de Montréal, Département de Physique, C.P. 6128 Succ. Centre-ville, Montréal, QC, H3C 3J7, Canada

³ Institut de Recherche sur les Exoplanètes (iREx), Université de Montréal, Département de Physique, C.P. 6128 Succ. Centre-ville, Montréal, QC, H3C 3J7, Canada

⁴ Department of Physics and Astronomy, The University of Western Ontario, 1151 Richmond Street, London, ON, N6A 3K7, Canada

⁵ Harvard-Smithsonian Center for Astrophysics, 60 Garden Street, Cambridge, MA, 02138, USA

⁶ National Radio Astronomy Observatory, 520 Edgemont Rd., Charlottesville, VA, 22903, USA

⁷ Department of Physics and Astronomy, University of Victoria, Victoria, BC, V8P 1A1, Canada

⁸ NRC Herzberg Astronomy and Astrophysics, 5071 West Saanich Rd, Victoria, BC, V9E 2E7, Canada

⁹ East Asian Observatory, 660 N. A'ohōkū Place, University Park, Hilo, HI 96720, USA

¹⁰ National Astronomical Observatory of Japan, National Institutes of Natural Sciences, Osawa, Mitaka, Tokyo 181-8588, Japan

¹¹ Korea Astronomy and Space Science Institute, 776 Daedeokdae-ro, Yuseong-gu, Daejeon 34055, Republic of Korea

¹² Korea University of Science and Technology, 217 Gajang-ro, Yuseong-gu, Daejeon 34113, Republic of Korea

¹³ Institute of Astronomy and Department of Physics, National Tsing Hua University, Hsinchu 30013, Taiwan

¹⁴ Academia Sinica Institute of Astronomy and Astrophysics, P.O. Box 23-141, Taipei 10617, Taiwan

¹⁵ School of Astronomy and Space Science, Nanjing University, 163 Xianlin Avenue, Nanjing 210023, China

¹⁶ Key Laboratory of Modern Astronomy and Astrophysics (Nanjing University), Ministry of Education, Nanjing 210023, China

¹⁷ Jeremiah Horrocks Institute, University of Central Lancashire, Preston PR1 2HE, United Kingdom

¹⁸Department of Physics and Astronomy, The University of Manitoba, Winnipeg, MB, R3T 2N2, Canada

¹⁹Physics and Astronomy, University of Exeter, Stocker Road, Exeter, EX4 4QL, United Kingdom

²⁰Department of Physics and Atmospheric Science, Dalhousie University, Halifax, NS, B3H 4R2, Canada

²¹Department of Physics and Astronomy, McMaster University, Hamilton, ON, L8S 4M1, Canada

²²Laboratoire AIM CEA/DSM-CNRS-Université Paris Diderot, IRFU/Service d'Astrophysique, CEA Saclay, F-91191 Gif-sur-Yvette, France

²³Department of Physics, Graduate School of Science, Nagoya University, Furo-cho, Chikusa-ku, Nagoya 464-8602, Japan

²⁴Department of Astronomy, Graduate School of Science, The University of Tokyo, 7-3-1 Hongo, Bunkyo-ku, Tokyo 113-0033, Japan

²⁵Institute of Astronomy, National Central University, Chung-Li 32054, Taiwan

²⁶National Astronomical Observatories, Chinese Academy of Sciences, A20 Datun Road, Chaoyang District, Beijing 100012, China

²⁷Department of Astronomy and Space Science, Chungnam National University, 99 Daehak-ro, Yuseong-gu, Daejeon 34134, Republic of Korea

²⁸School of Physics, Astronomy & Mathematics, University of Hertfordshire, College Lane, Hatfield, Hertfordshire AL10 9AB, UK

²⁹Department of Earth Science and Astronomy, Graduate School of Arts and Sciences, The University of Tokyo, 3-8-1 Komaba, Meguro, Tokyo 153-8902, Japan

³⁰School of Physics and Astronomy, Cardiff University, The Parade, Cardiff, CF24 3AA, UK

³¹Jet Propulsion Laboratory, M/S 169-506, 4800 Oak Grove Drive, Pasadena, CA 91109, USA

³²Jeremiah Horrocks Institute, University of Central Lancashire, Preston PR1 2HE, UK

³³Department of Applied Mathematics, University of Leeds, Woodhouse Lane, Leeds LS2 9JT, UK

³⁴Jodrell Bank Centre for Astrophysics, School of Physics and Astronomy, University of Manchester, Oxford Road, Manchester, M13 9PL, UK

³⁵Tokushima University, Minami Jousanajima-machi 1-1, Tokushima 770-8502, Japan

³⁶Institute of Liberal Arts and Sciences Tokushima University, Minami Jousanajima-machi 1-1, Tokushima 770-8502, Japan

³⁷Department of Physics, The Chinese University of Hong Kong, Shatin, N.T., Hong Kong

³⁸Subaru Telescope, National Astronomical Observatory of Japan, 650 N. A'ohōkū Place, Hilo, HI 96720, USA

³⁹UK Astronomy Technology Centre, Royal Observatory, Blackford Hill, Edinburgh EH9 3HJ, UK

⁴⁰Institute for Astronomy, University of Edinburgh, Royal Observatory, Blackford Hill, Edinburgh EH9 3HJ, UK

⁴¹Department of Environmental Systems Science, Doshisha University, Tatara, Miyakodani 1-3, Kyotanabe, Kyoto 610-0394, Japan

⁴²Division of Theoretical Astronomy, National Astronomical Observatory of Japan, Mitaka, Tokyo 181-8588, Japan

⁴³Hiroshima Astrophysical Science Center, Hiroshima University, Kagamiyama 1-3-1, Higashi-Hiroshima, Hiroshima 739-8526, Japan

⁴⁴Department of Physics, Hiroshima University, Kagamiyama 1-3-1, Higashi-Hiroshima, Hiroshima 739-8526, Japan

⁴⁵Core Research for Energetic Universe (CORE-U), Hiroshima University, Kagamiyama 1-3-1, Higashi-Hiroshima, Hiroshima 739-8526, Japan

⁴⁶Nobeyama Radio Observatory, National Astronomical Observatory of Japan, National Institutes of Natural Sciences, Nobeyama, Minamimaki, Minamisaku, Nagano 384-1305, Japan

⁴⁷Department of Earth Science Education, Kongju National University, 56 Gongjudaehak-ro, Gongju-si 32588, Republic of Korea

⁴⁸Institute of Space and Astronautical Science, Japan Aerospace Exploration Agency, 3-1-1 Yoshinodai, Chuo-ku, Sagamihara, Kanagawa 252-5210, Japan

⁴⁹School of Space Research, Kyung Hee University, 1732 Deogyeong-daero, Giheung-gu, Yongin-si, Gyeonggi-do 17104, Republic of Korea

⁵⁰Xinjiang Astronomical Observatory, Chinese Academy of Sciences, 150 Science 1-Street, Urumqi 830011, Xinjiang, China

⁵¹School of Physics and Astronomy, University of Leeds, Woodhouse Lane, Leeds LS2 9JT, UK

⁵²Kagawa University, Saiwai-cho 1-1, Takamatsu, Kagawa, 760-8522, Japan

⁵³Department of Astronomy, Graduate School of Science, Kyoto University, Sakyo-ku, Kyoto 606-8502, Japan

⁵⁴SOKENDAI (The Graduate University for Advanced Studies), Hayama, Kanagawa 240-0193, Japan

⁵⁵Kagoshima University, 1-21-35 Korimoto, Kagoshima, Kagoshima 890-0065, Japan

⁵⁶Astrophysics Group, Cavendish Laboratory, J J Thomson Avenue, Cambridge CB3 0HE, UK

⁵⁷Kavli Institute for Cosmology, Institute of Astronomy, University of Cambridge, Madingley Road, Cambridge, CB3 0HA, UK

⁵⁸Université Grenoble Alpes, CNRS, IPAG, 38000 Grenoble, France

⁵⁹Department of Astronomy and Earth Sciences, Tokyo Gakugei University, Koganei, Tokyo 184-8501, Japan

⁶⁰OSL, Physics & Astronomy Dept., University College London, WC1E 6BT London, UK

⁶¹Department of Physics, School of Science and Technology, Kwansei Gakuin University, 2-1 Gakuen, Sanda, Hyogo 669-1337, Japan

⁶²Purple Mountain Observatory, Chinese Academy of Sciences, 2 West Beijing Road, 210008 Nanjing, PR China

⁶³European Southern Observatory (ESO), Karl-Schwarzschild-Strae 2, D-85748 Garching, Germany

(Received August 21, 2018; Revised December 11, 2021)

Submitted to ApJ

ABSTRACT

We present the POL-2 850 μm linear polarization map of the Barnard 1 clump in the Perseus molecular cloud complex from the B-fields In STar-forming Region Observations (BISTRO) survey at the James Clerk Maxwell Telescope. We find a trend of decreasing polarization fraction as a function of total intensity, which we link to depolarization effects towards higher density regions of the cloud. We then use the polarization data at 850 μm to infer the plane-of-sky orientation of the large-scale magnetic field in Barnard 1. This magnetic field runs North-South across most of the cloud, with the exception of B1-c where it turns more East-West. From the dispersion of polarization angles, we calculate a turbulence correlation length of 5.0 ± 2.5 arcsec (1500 au), and a turbulent-to-total magnetic energy ratio of 0.5 ± 0.3 inside the cloud. We combine this turbulent-to-total magnetic energy ratio with observations of NH₃ molecular lines from the Green Bank Ammonia Survey (GAS) to estimate the strength of the plane-of-sky component of the magnetic field through the Davis-Chandrasekhar-Fermi method. With a plane-of-sky amplitude of $120 \pm 60 \mu\text{G}$ and a criticality criterion $\lambda_c = 3.0 \pm 1.5$, we find that Barnard 1 is a supercritical molecular cloud with a magnetic field nearly dominated by its turbulent component.

Keywords: stars: formation — polarization — ISM: magnetic fields — ISM: clouds — submillimeter: ISM — ISM: individual objects: Barnard 1

1. INTRODUCTION

Magnetic fields, which are ubiquitous within the Galaxy (e.g., [Ordog et al. 2017](#); [Planck Collaboration et al. 2015a](#)), influence greatly the stability of molecular clouds and their dense filamentary structures in which star formation occurs (e.g., [André et al. 2014](#); [André 2015](#)). Specifically, magneto-hydrodynamic simulations have shown that a combination of magnetism and turbulence is needed to slow the gravitational collapse of molecular clouds, and thus decrease the galactic star formation rate (e.g., [Padoan et al. 2014](#)). Measuring the amplitude of magnetic fields in dense interstellar environments is therefore crucial to our understanding of the physical processes leading to the formation of stars and their planets.

Interstellar magnetic fields are difficult to observe directly. Early studies hypothesized that polarization of background starlight through the interstellar medium was due to the alignment of irregularly-shaped dust grains with magnetic field lines ([Hiltner 1949](#)). Subsequent observations of thermal dust emission in the far-infrared ([Cudlip et al. 1982](#)) showed polarization orientations nearly orthogonal to measurements in the near-infrared, supporting the picture of elongated dust grains. Although magnetic fields are considered the most likely cause of dust alignment in interstellar environments, the grain alignment mechanisms themselves still remain a theoretical challenge (e.g., [Andersson et al. 2015](#), and references therein).

The Radiative Alignment Torque (RAT) theory of grain alignment is currently one of the most promising models to explain the polarization of starlight towards clouds and cores ([Lazarian 2007](#)). In summary, this model predicts that asymmetric, non-spherical dust grains rotate due to radiative torques from their local radiation field and then align themselves with their long axis perpendicular to the ambient magnetic field ([Dolginov & Mitrofanov 1976](#); [Draine & Weingartner 1997](#); [Weingartner & Draine 2003](#); [Lazarian & Hoang 2007a](#)). The degree of this alignment, however, depends on the quantity of paramagnetic material in the dust ([Hoang & Lazarian 2016](#)). Submillimeter polarization observations of optically thin thermal dust emission will therefore lie perpendicular to the plane-of-sky component of the field.

The B-fields In STar-forming Region Observations (BISTRO) survey aims to study the role of magnetism for the formation of stars in the dense filamentary structures of giant molecular clouds ([Ward-Thompson et al. 2017](#)). This goal will be achieved by mapping the $850\text{ }\mu\text{m}$ linear polarization towards at least 16 fields (for a total of 224 hours) in nearby star-forming regions

with the newly commissioned polarimeter POL-2 at the James Clerk Maxwell Telescope (JCMT). With the unprecedented single dish sensitivity of the Sub-millimetre Common-User Bolometer Array 2 (SCUBA-2) camera on which POL-2 is installed, the BISTRO survey will significantly expand on previously obtained polarization measurements at submillimeter and millimeter wavelengths (e.g., [Matthews et al. 2009](#); [Dotson et al. 2010](#); [Vaillancourt & Matthews 2012](#); [Hull et al. 2014](#); [Koch et al. 2014](#); [Zhang et al. 2014](#)).

Several of the star-forming regions observed by BISTRO are part of the Gould Belt, a ring of active star-forming regions approximately 350 pc-across that is centered roughly 200 pc from the Sun ([Gould 1879](#)). Here, we present the BISTRO observations of the Barnard 1 clump (hereafter Perseus B1, or B1) in the Perseus molecular cloud ($d \sim 295$ pc; [Ortiz-León et al. 2018](#)). B1 is known to host several prestellar and protostellar cores at different evolutionary stages (e.g., [Hirano et al. 1997, 1999](#); [Matthews et al. 2006](#); [Pezzuto et al. 2012](#); [Carney et al. 2016](#)). This cloud was also a target of both the JCMT and *Herschel* Gould Belt surveys (from $70\text{ }\mu\text{m}$ to $850\text{ }\mu\text{m}$), thus providing a characterization of its dust properties ([Sadavoy et al. 2013](#); [Chen et al. 2016](#)).

This paper presents the BISTRO first-look analysis of the Perseus B1 star-forming region. In Section 2, we first describe the technical details of the polarization observations, and outline the spectroscopic data used in this work. In Section 3, we show the POL-2 $850\text{ }\mu\text{m}$ linear polarization map of B1 and its inferred plane-of-sky magnetic field morphology. We also characterize the relationship between the polarization fraction and the total intensity, and we compare the POL-2 data with previous SCUPOL observations. In Section 4, we explain our methodology for measuring the magnetic field strength from the polarization data, and then present the results of this analysis. In Section 5, we discuss the significance of these results for the role of the magnetic field on star formation within Perseus B1. Finally, we summarize our findings in Section 6.

2. OBSERVATIONS

2.1. *Polarimetric Data*

The JCMT is a submillimeter observatory equipped with a 15 m dish that is located at an altitude of 4,092 m on top of Maunakea in Hawaii, USA. Its continuum instrument is SCUBA-2, a cryogenic 10,000 pixel camera capable of simultaneous observing in the $450\text{ }\mu\text{m}$ and the $850\text{ }\mu\text{m}$ atmospheric windows ([Holland et al. 2013](#)). The SCUBA-2 beams can be approximated by a two-dimensional Gaussian with a full-width

at half-maximum (FWHM) of 9.6 arcsec at 450 μm and 14.6 arcsec at 850 μm (Dempsey et al. 2013).

The POL-2 polarimeter consists of a rotating half-wave plate and a fixed polarizer placed in the optical path of the SCUBA-2 camera (Bastien et al. 2011; Friberg et al. 2016; P. Bastien et al. in prep.). POL-2 is the follow-up instrument to the SCUBA polarimeter (SCUPOL), which had a similar basic design (Greaves et al. 2003). While SCUBA-2 always simultaneously observes at both 450 μm and 850 μm , only the 850 μm capabilities of POL-2 were commissioned at the time of writing. In brief, POL-2 observes by scanning the sky at a speed of 8 arcsec s^{-1} in a daisy-like pattern over a field that is roughly 11 arcmin in diameter. Since the half-wave plate is rotated at a rate of 2 Hz, this scanning rate ensures a full rotation of the half-wave plate for every measurement of a 4 arcsec box position in the map. For this paper, the Flux Calibration Factor (FCF) of POL-2 at 850 μm is assumed to be 725 Jy pW^{-1} beam $^{-1}$ for each of the Stokes I , Q , and U parameters (the Stokes parameters are defined in Section 3.1). This value was determined by multiplying the typical SCUBA-2 FCF of 537 Jy pW^{-1} beam $^{-1}$ (Dempsey et al. 2013) with a transmission correction factor of 1.35 measured in the laboratory and confirmed empirically by the POL-2 commissioning team using observations of the planet Uranus (Friberg et al. 2016).

Perseus B1 was observed with POL-2 between 2016 September and 2017 March as part of the BISTRO large program at the JCMT (project ID: M16AL004). These observations total 14 hours (or 20 individual sets of \sim 40-minutes observations) of integration in Grade 2 weather (i.e., for a 225 GHz atmospheric opacity, τ_{225} , between 0.05 and 0.08). A 20-minute SCUBA-2 scan of B1 without POL-2 in the beam was also obtained on 2016 September 8 to serve as a reference for pointing corrections during data reduction.

The data were reduced using the STARLINK (Currie et al. 2014) procedure *pol2map* (Parsons et al. 2017), which is adapted from the SCUBA-2 data reduction procedure *makemap* (Chapin et al. 2013). In particular, this routine is used to reduce POL-2 time-series observations into Stokes I , Q , and U maps. We follow the convention set by the International Astronomical Union (IAU) for the definition of Stokes parameters. The default pixel size of the maps produced by *pol2map* is 4 arcsec. For the analysis presented in this paper, we have instead chosen a pixel size of 12 arcsec at the start of the data reduction process to improve the resulting signal-to-noise ratio (SNR) of the final Stokes I , Q , and U maps.

The data reduction process is divided into three steps to optimize the SNR in the resulting maps: (1) the pro-

cedure *pol2map* is run a first time without applying any masks to obtain an initial Stokes I intensity map directly from the POL-2 time-series observations; (2) this initial Stokes I map is then used as the reference for the automatic masking process of *pol2map*, which is run a second time on the time-series observations to produce the final Stokes I map; and (3) the masks obtained in Step 2 are also applied during a third run of *pol2map* to reduce the Stokes Q and U maps, which are automatically corrected for the instrumental polarization. The uncertainties in each pixel of the Stokes I , Q , and U maps are taken directly from the variance maps provided by the *pol2map* procedure. The role of masking in the reduction of SCUBA-2 data, and incidentally POL-2 data, is discussed at length by Mairs et al. (2015).

The correction for instrumental polarization is a crucial step in the analysis of any polarization measurement. If the instrumental polarization is not properly taken into account, then it may lead to erroneous results. For this reason, the latest model (January 2018) for the instrumental polarization of the JCMT at 850 μm was extensively tested by the POL-2 commissioning team with observations of Uranus and Mars (Friberg et al. 2016, 2018; P. Bastien et al., in prep.). They found that the instrumental polarization can be accurately described using a two-components model combining the optics of the telescope and its protective wind blind. While the level of instrumental polarization is dependent on elevation, it is typically ~ 1.5 per cent of the measured total intensity (Friberg et al. 2018).

We also use 850 μm polarization data of Perseus B1 from the SCUPOL Legacy Catalog. Matthews et al. (2009) built this legacy catalog by systematically reducing SCUPOL 850 μm observations towards 104 regions, including previously published observations of B1 (Matthews & Wilson 2002), to provide reference Stokes cubes of comparable quality for all the astronomical sources with at least a 2 sigma detection of polarization. For this paper, the SCUPOL Stokes I , Q , and U cubes for B1 were downloaded from the legacy catalog's online archive hosted by the CADC. To match the POL-2 results, we resampled the SCUPOL polarization vectors onto a 12 arcsec pixel grid.

2.2. Spectroscopic Data

The JCMT is also equipped with the HARP/ACSIIS high-resolution heterodyne spectrometer capable of observing molecular lines between 325 GHz and 375 GHz (or 922 μm to 799 μm). The Heterodyne Array Receiver Program (HARP) is a 4×4 detector array that can be used in combination with the Auto-Correlation Spectral Imaging System (ACSIIS) to rapidly produce large-

scale velocity maps of astronomical sources (Buckle et al. 2009). In this paper, we use the previously published ~ 14 arcsec resolution integrated intensity map of the ^{12}CO J=3-2 molecular line towards Perseus B1 (project ID: S12AC01) (Sadavoy et al. 2013). This intensity map was integrated over a bandwidth of 1.0 GHz centered on the rest frequency of the ^{12}CO J=3-2 line at 345.796 GHz. The noise added by integrating over such a large bandwidth has no effect on the results presented in this work since the ^{12}CO J=3-2 data is used only to indicate the presence of outflows in Figure 1.

It is important to note that SCUBA-2, POL-2, and HARP are not sensitive to exactly the same spatial scales. This difference is due to a combination of the different scanning strategies for each instrument and their associated data reduction procedures (e.g., Chapin et al. 2013). Hence, this difference must be kept in mind when combining results from different instruments, such as correcting for molecular contamination using HARP or comparing source intensities between POL-2 and SCUBA-2. While this difference is not an issue for the results presented in this paper, it may need to be taken into account in future studies using BISTRO data (see Section A for more details).

Finally, this project makes use of spectroscopic data from the Green Bank Ammonia Survey (GAS) (Friesen et al. 2017). GAS uses the K-Band Focal Plane Array (KFPA) and the VErsatile GBT Astronomical Spectrometer (VEGAS) at the Green Bank Telescope (GBT) to map ammonia lines, among others, in nearby star-forming regions. In this work, we specifically use measurements of the NH_3 (1,1) and (2,2) lines towards Perseus B1 (GAS Consortium, in prep.). These observations of NH_3 molecular lines at ~ 23.7 GHz have a spatial resolution of 32 arcsec and a velocity resolution of ~ 0.07 km s $^{-1}$.

3. RESULTS

3.1. Polarization Properties

The polarization vectors are defined by the polarization fraction P and the polarization angle Φ measured eastward from celestial North. These properties are determined directly from the Stokes I , Q , and U parameters, which is the commonly accepted parametrization for partially polarized light. The Stokes I parameter is the total intensity of the incoming light, and the Stokes Q and U parameters are respectively defined as $Q = I P \cos(2\Phi)$ and $U = I P \sin(2\Phi)$.

When Q and U are near zero, these values will be dominated by the noise in our measurements. This noise contribution always leads to a positive bias in the calculation of the polarization fraction P due to the quadratic

nature of the polarized intensity $I_P = [Q^2 + U^2]^{1/2}$ (e.g., Wardle & Kronberg 1974; Montier et al. 2015; Vidal et al. 2016). The amplitude of this positive bias can be approximated from the uncertainty σ_{I_P} given in Equation 2, which is used in Equation 1 to de-bias the polarization fraction P (e.g., Naghizadeh-Khouei & Clarke 1993).

The de-biased polarization fraction P (in per cent) can therefore be written as:

$$P = \frac{100}{I} \sqrt{Q^2 + U^2 - \sigma_{I_P}^2} = \frac{100}{I} I_P, \quad (1)$$

where we re-define I_P as the de-biased polarized intensity with uncertainty σ_{I_P} . This uncertainty σ_{I_P} is given by:

$$\sigma_{I_P} = \left[\frac{(Q \sigma_Q)^2 + (U \sigma_U)^2}{Q^2 + U^2} \right]^{1/2}, \quad (2)$$

where σ_Q and σ_U are the uncertainties on the Stokes Q and U parameters respectively. The uncertainty σ_P of the polarization fraction P is given by:

$$\sigma_P = P \left[\left(\frac{\sigma_{I_P}}{I_P} \right)^2 + \left(\frac{\sigma_I}{I} \right)^2 \right]^{1/2}, \quad (3)$$

where σ_I is the uncertainty on the Stokes I total intensity.

Finally, the expression for the polarization angle Φ is:

$$\Phi = \frac{1}{2} \arctan \left(\frac{U}{Q} \right), \quad (4)$$

where Φ is defined between 0 and π (0° and 180°) for convenience, and its related uncertainty σ_Φ is given by:

$$\sigma_\Phi = \frac{1}{2} \sqrt{\frac{(U \sigma_Q)^2 + (Q \sigma_U)^2}{Q^2 + U^2}}. \quad (5)$$

3.2. BISTRO First-Look at Perseus B1

Figure 1 (left) shows the BISTRO 850 μm linear polarization map of Perseus B1 for a pixel size of 12 arcsec. The catalog of polarization vectors is calculated for every pixel of the POL-2 Stokes I , Q and U maps, but only vectors passing a set of pre-determined selection criteria are shown. These selection criteria are: a SNR of $I/\sigma_I > 3$ for Stokes I and its uncertainty σ_I , a SNR of $P/\sigma_P > 3$ for the polarization fraction P and its uncertainty σ_P , and an uncertainty $\sigma_P < 5$ per cent for the polarization fraction. The criterion of $\sigma_P < 5$ per cent was chosen arbitrarily as a precaution against potentially spurious vectors with anomalously high polarization fractions. These criteria provide a catalog of 224 polarization vectors for Perseus B1.

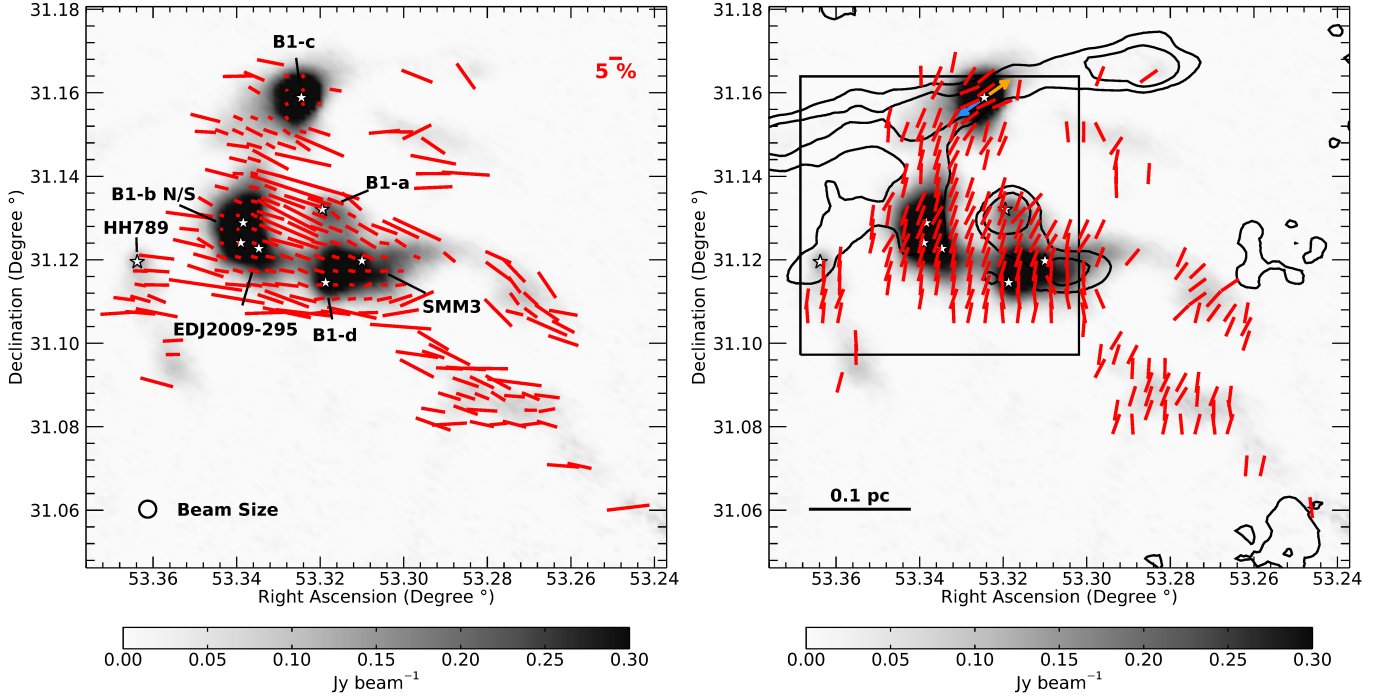


Figure 1. The Perseus B1 star-forming region in $850 \mu\text{m}$ dust polarization from POL-2. In each panel, the gray scale indicates the measured Stokes I total intensity. *Left:* Vectors show the $850 \mu\text{m}$ linear polarization measured with POL-2 for a pixel scale of 12 arcsec, which is comparable to the effective beam size. The length of each vector is determined by its associated polarization fraction P (per cent). The size of the SCUBA-2 beam at $850 \mu\text{m}$ (14.6 arcsec) is shown as a circle on the bottom left corner of the panel. Astronomical objects of interest are labeled and their positions are indicated by star symbols. *Right:* Vectors show the inferred plane-of-sky magnetic field morphology obtained from the 90° rotation of the polarization vectors, which are normalized by length for clarity. The black contours trace the integrated intensity (10 K km s^{-1} and 20 K km s^{-1}) of the ^{12}CO $J=3-2$ molecular line measured with HARP (Sadavoy et al. 2013). The blue and orange arrows around the protostellar core B1-c indicate the orientation of its blueshifted and redshifted outflows respectively, as characterized by Matthews et al. (2006). Each lobe shows a clear bi-modal component with a FWHM of 5 to 10 km s^{-1} , and the typical velocity range in B1 is between -5 and 5 km s^{-1} relative to the bulk of the cloud. The black box indicates the region analyzed for the improved Davis-Chandrasekhar-Fermi method described in Section 4.1. As a reference, the plain line drawn in the bottom left corner of the panel indicates a physical length of 0.1 pc .

The mean values of the Stokes uncertainties σ_I , σ_Q , and σ_U for the polarization vectors shown in Figure 1 are $1.6 \text{ mJy beam}^{-1}$, $1.3 \text{ mJy beam}^{-1}$, and $1.3 \text{ mJy beam}^{-1}$ respectively. At best, we achieve a sensitivity of 0.1 per cent in polarization fraction and an uncertainty of 2.1° in polarization angle, with mean values for σ_P of 1.9 per cent and for σ_Φ of 5.7° for the entire catalog of vectors.

Assuming that interstellar dust grains are aligned with their long axis perpendicular to the magnetic field, the plane-of-sky field morphology in Perseus B1 is obtained by rotating the vectors in the polarization map by 90° . Figure 1 (right) shows the inferred plane-of-sky magnetic field map for B1. To help highlight the magnetic field structure, the rotated vectors are normalized to the same length. A contour plot of the HARP ^{12}CO $J=3-2$ integrated intensity map from the JCMT Gould Belt Survey (Sadavoy et al. 2013) is also included in the right panel of Figure 1.

Selected submillimeter sources are identified in both panels of Figure 1 to serve as references for the discussion in Section 5 (Bally et al. 2008). These sources are embedded young stellar objects which have been associated with molecular outflows (Hatchell & Dunham 2009; Evans et al. 2009; Hirano & Liu 2014; Carney et al. 2016). Specifically, the lobes of the precessing molecular outflow originating from the protostellar core B1-c (Matthews et al. 2006) are particularly well defined by the ^{12}CO $J=3-2$ contour plot shown in the right panel of Figure 1.

The top panel of Figure 2 compares the fraction of polarization P with the Stokes I total intensity for each of the POL-2 vectors shown on the left panel of Figure 1. There is a clear trend of decreasing fraction P as a function of increasing Stokes I . If the total intensity is correlated with the column density (Hildebrand 1983), this behavior can be understood as the result of

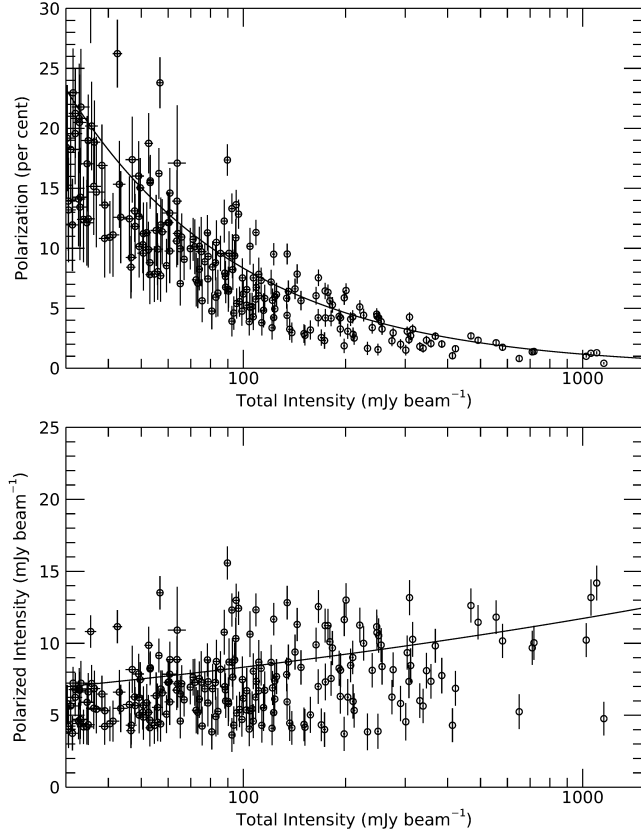


Figure 2. Depolarization of POL-2 observations towards Perseus B1. Each point represents one of the polarization vectors shown in the left panel of Figure 1. The vertical and horizontal lines show the uncertainties for the plotted parameters in each panel. *Top*: De-biased polarization fraction P as a function of the Stokes I total intensity. *Bottom*: De-biased polarized intensity I_P as a function of the Stokes I total intensity. The solid line in the top panel is the power-law fit (with index $\alpha \sim -0.85$) between the polarization fraction P and the Stokes I total intensity ($P \propto I^\alpha$, see Section 3.2). The solid line in the bottom panel is the same power-law fit as above, but multiplied by the Stokes I total intensity ($I_P \propto I^{\alpha+1}$).

a depolarization effect towards higher density regions of the cloud. The origin of this depolarization effect is discussed in Section 5. This trend does not mean, however, that the polarized intensity I_P itself is decreasing. Indeed, the bottom panel of Figure 2 shows that I_P may be in fact increasing slowly with Stokes I .

We fitted a power-law ($P \propto I^\alpha$) to the data in Figure 2 (top) using an error-weighted least-square minimization technique. We find a power index $\alpha = -0.85 \pm 0.01$, with a reduced chi-squared $\chi^2_r = 3.4$. This power-law is shown in both panels of Figure 2 as a solid line. The spread of data points relative to their uncertainties is responsible for the large χ^2_r value obtained, which indicates that fitting a single power-law may not be sufficient

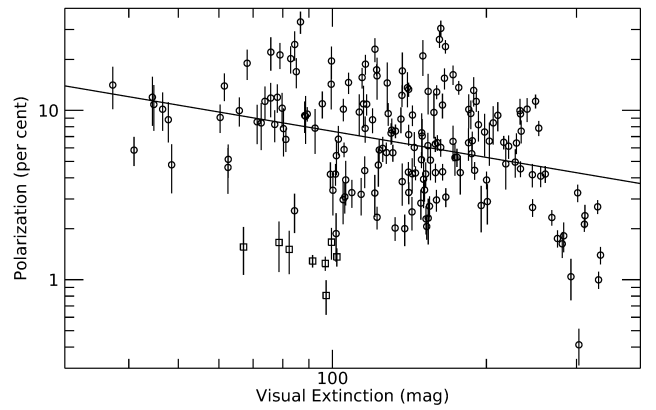


Figure 3. Relationship between the de-biased polarization fraction P and the visual extinction A_V in Perseus B1. Each point represents one of the polarization vectors from the left panel of Figure 1 that also have *Herschel*-derived opacity measurements. The visual extinction A_V is derived from the $300 \mu\text{m}$ τ_{300} opacity map from Chen et al. (2016) assuming a reddening factor $R_V = 3.1$. The figure covers a range of extinction A_V from 30 mag to 400 mag. The vertical lines show the uncertainties for the polarization fraction P . The 8 polarization vectors found towards B1-c are identified with squares. The solid line is the power-law fit (with index $\beta \sim -0.5$) between the polarization fraction P and the visual extinction A_V ($P \propto A_V^\beta$, see Section 3.2).

to account for the entire data set. The detailed effects of measurement uncertainties on the power-law fit between P and I are currently under investigation (K. Pattle et al., in prep.).

The power index $\alpha \sim -0.85$ we find for B1 is nearly identical to the value measured in ρ Ophiuchus B by Soam et al. (2018) and relatively close to the index $\alpha \sim -0.8$ measured by Kwon et al. (2018) in ρ Ophiuchus A, both obtained from BISTRO data. Similarly, Matthews & Wilson (2002) previously found a power index $\alpha \sim -0.8$ in B1 using SCUPOL 850 μm measurements. The differences between POL-2 and SCUPOL polarization maps of B1 are quantified in Section 3.3.

However, in the context of grain alignment theory, it is more meaningful to take the optical depth into account when studying depolarization effects in molecular clouds. While an accurate modeling of the alignment efficiency of dust grains in Perseus B1 will require a detailed analysis beyond the scope of this work, we can nonetheless begin to characterize the relationship between the polarized dust thermal emission and the visual extinction A_V in the cloud by fitting a power-law of the form $P \propto A_V^\beta$ (e.g., Alves et al. 2014). Specifically, we know that the polarization fraction P of dust thermal emission obtained from submillimeter observations is proportional to the polarization efficiency

P_{ext}/A_V derived from measurements of the polarization fraction P_{ext} due to extinction at visible wavelengths (Andersson et al. 2015).

Figure 3 shows the relation between the polarization fraction P and the derived visual extinction A_V for the polarization vectors shown the left panel of Figure 1 that also have an associated opacity measurement in the $300\ \mu\text{m}$ τ_{300} opacity map from Chen et al. (2016). We estimate the visual extinction A_V using Equation A5 from Jones et al. (2015) and a version of the τ_{300} opacity map from Chen et al. (2016) that has been re-gridded from a pixel scale of 14 arcsec to 12 arcsec to match our observations. We also assume a reddening R_V of 3.1 which may be more representative of the diffuse interstellar medium (Weingartner & Draine 2001), but should nonetheless serve as a reasonable lower limit for our estimation of the visual extinction A_V across the cloud.

We fitted a power-law $P \propto A_V^\beta$ to the data shown in Figure 3 using an error-weighted least-square minimization technique. We find a power index $\beta = -0.51 \pm 0.03$, with a reduced chi-squared $\chi_r^2 = 26.3$. This power-law is shown in Figure 3 as a solid line. The large reduced chi-squared χ_r^2 value we find clearly indicates a poor fit to the data considering the spread of values and their uncertainties for the polarization fraction P in Figure 3. This could be explained in part by our use of a single reddening value to derive the visual extinction A_V . Indeed, the reddening R_V depends on the size distribution and composition of the dust grains, and so we do not expect this value to be constant across the cloud.

Nevertheless, the power index $\beta \sim -0.5$ we find in B1 is shallower than the power indices obtained from submillimeter observations in the Pipe-109 starless core ($\beta \sim -0.9$, Alves et al. 2014, 2015) and in the LDN 183 starless core ($\beta \sim -1.0$, Andersson et al. 2015). In fact, a power index $\beta \sim -0.5$ is closer to the power index $\beta \sim -0.6$ measured towards lower extinction regions ($A_V < 20$) of LDN 183 using visible and near-infrared observations (Andersson et al. 2015). Although Figure 2 clearly shows a depolarization effect with increasing total intensity I , the power index $\beta \sim -0.5$ we find using the data in Figure 3 suggests that dust grains in Perseus B1 are aligned more efficiently than in starless cores with comparable measures of visual extinction A_V . Since B1 is a site of on-going star formation, this may provide evidence that radiation from embedded young stellar objects can compensate for the expected loss of grain alignment with increasing visual extinction.

3.3. Comparison with SCUPOL Legacy Data

As mentioned in Section 2.1, Perseus B1 was previously observed at $850\ \mu\text{m}$ with the SCUPOL polarimeter

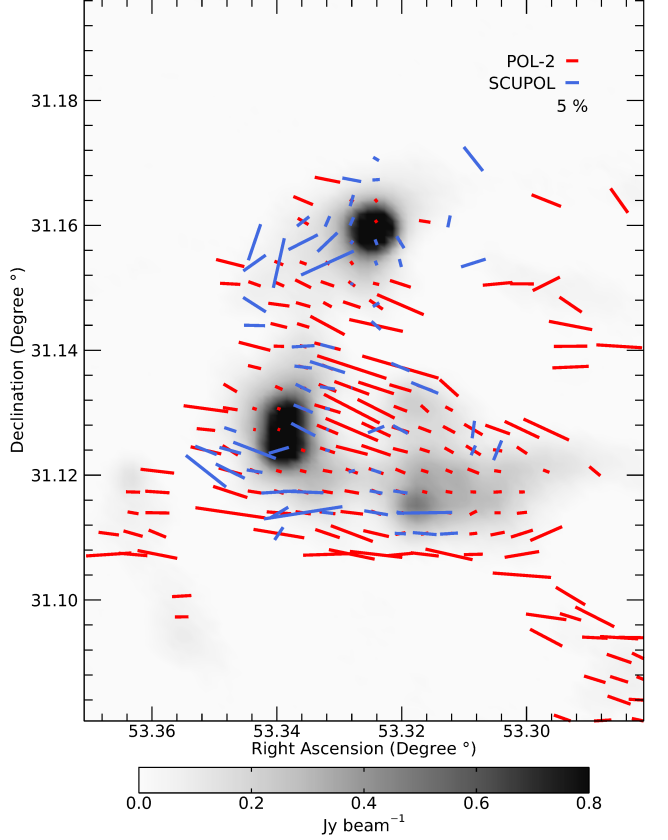


Figure 4. Comparison of dust polarization at $850\ \mu\text{m}$ between POL-2 (red) and SCUPOL (blue) towards Perseus B1. The gray scale indicates the Stokes I total intensity measured with POL-2. The length of each vector is determined by its associated polarization fraction P (per cent). The SCUPOL polarization vectors from Matthews et al. (2009) have been re-binned to match the exact position and pixel scale (from 10 arcsec to 12 arcsec) of the POL-2 observations.

(Matthews & Wilson 2002). Here we specifically compare the BISTRO results presented in Section 3.2 to the polarization data of B1 found in the SCUPOL Legacy Catalog (Matthews et al. 2009).

Figure 4 compares the BISTRO observations to their equivalent data set in the SCUPOL Legacy Catalog, with the POL-2 polarization vectors (same as Figure 1) in red and the SCUPOL vectors in blue. To have a significant number of SCUPOL vectors for this comparison, we relaxed their selection criteria compared to POL-2. For the SCUPOL data, we use $I/\sigma_I > 2$, $P/\sigma_P > 2$, and $\sigma_P < 10$ per cent. These relaxed criteria provide a total catalog of 69 vectors, compared to only 17 when applying the same selection criteria as for the POL-2 data.

At best, the relaxed catalog of SCUPOL vectors achieves a sensitivity of 0.5 per cent in polarization fraction and an uncertainty of 5.5° in polarization angle,

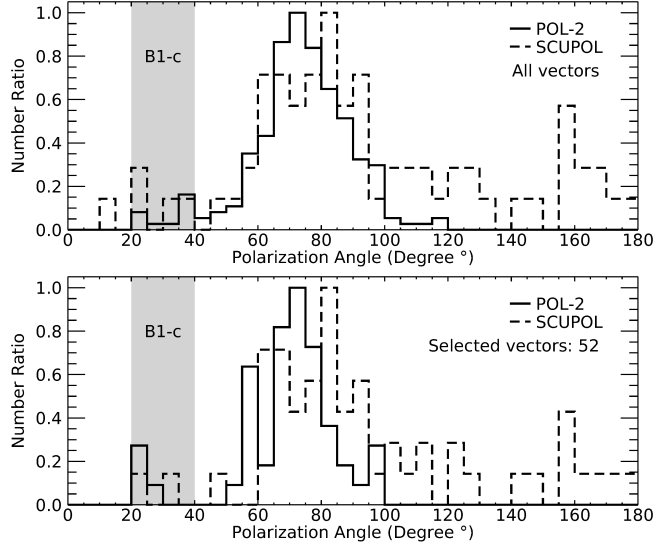


Figure 5. Histograms of polarization angles for Perseus B1 from POL-2 and SCUPOL. The number of vectors in each bin is normalized by the maximum value of the histogram ($N_{\text{bin}}/N_{\text{max}}$) for a given sample of polarization angles. *Top:* Histogram including all the POL-2 (224) and SCUPOL (69) polarization vectors shown in Figure 1 and Figure 4 respectively. *Bottom:* Histogram including only the 52 positions for which there exists both a POL-2 and a SCUPOL polarization vector in Figure 4. In both panels, the range of polarization angles associated with the protostellar source B1-c is shown in gray.

with mean values for σ_P of 2.7 per cent and for σ_Φ of 10.3°.

Figure 5 shows the distribution of angles for both the POL-2 and SCUPOL polarization maps. The top panel shows the histogram including all the POL-2 and SCUPOL polarization vectors shown in Figure 4, normalized by the maximum value in each distribution. Both distributions peak between 65° and 85°. The bottom panel shows the normalized distributions only for those vector positions that are common (i.e., spatially overlapping within the same pixel) to both SCUPOL and POL-2. There are 52 such positions in the maps.

We used a Kolmogorov-Smirnov test to compare the distributions shown at the bottom of Figure 5. Specifically, a two-sample Kolmogorov-Smirnov test provides the probability that two independent data samples are drawn from the same intrinsic distribution by measuring the maximum distance between the cumulative probability distribution of each sample. For example, if both the SCUPOL and POL-2 values for the selected co-spatial vectors were exact measurements of the 850 μm polarization towards Perseus B1, then we would expect the two catalogs of polarization angles, and therefore their respective cumulative probability distributions, to

be identical and the Kolmogorov-Smirnov test to return a 100 per cent probability that they are drawn from the same intrinsic distribution of polarization angles. In reality, the POL-2 and SCUPOL distributions shown in the bottom panel of Figure 5 are not identical even though they probe the same positions in B1, and so the Kolmogorov-Smirnov test becomes a way of quantifying the difference between them since it makes no assumption about the nature of the aforementioned intrinsic distribution.

In this case, we find a low likelihood (0.6 per cent) that both POL-2 and SCUPOL distributions in the bottom panel of Figure 5 are drawn from the same intrinsic distribution of polarization angles (with a maximum deviation $D = 0.39$ between the cumulative probability distributions). In other words, based only on the 52 available co-spatial vectors in each sample, a two-sample Kolmogorov-Smirnov test shows that the distributions of POL-2 and SCUPOL polarization angles are significantly different from each other. If we set the selection criteria for POL-2 vectors to be identical to those applied for SCUPOL vectors, we find instead 64 positions with vectors common to both catalogs. This relaxed data set does not, however, improve the results of the Kolmogorov-Smirnov test.

Figure 6 expands the comparison shown in Figure 5 (bottom) between the POL-2 and SCUPOL polarization angles for pairs of spatially overlapping vectors. The top panel of Figure 6 shows that most outliers from the 1:1 correspondence line are found towards lower intensity regions ($I < 200 \text{ mJy beam}^{-1}$), as measured from POL-2 Stokes I . Furthermore, in Figure 6 (bottom), the vector pairs displaying the largest angular difference ($|\Phi_{\text{SCUPOL}} - \Phi_{\text{POL-2}}|$) are found near or below a SNR of 3 for the polarization fraction ($P_{\text{SCUPOL}}/\sigma_{P_{\text{SCUPOL}}} \lesssim 3$) measured with SCUPOL. Although the pairs of vectors at high SNR ($P_{\text{SCUPOL}}/\sigma_{P_{\text{SCUPOL}}} > 4$) also exhibit a non-negligible angular difference, this effect is not nearly as pronounced as for the low SNR vectors ($P_{\text{SCUPOL}}/\sigma_{P_{\text{SCUPOL}}} \lesssim 3$). This disparity between POL-2 and SCUPOL could therefore be explained by the relatively high noise levels in the SCUPOL Legacy data.

4. ANALYSIS

4.1. Angular Dispersion Analysis and Davis-Chandrasekhar-Fermi Method

The magnetic field strength in molecular clouds can be estimated through the Davis-Chandrasekhar-Fermi (DCF) method (Davis 1951; Chandrasekhar & Fermi 1953). This technique relies on the assumption that turbulent motions in the gas will locally inject randomness in the observed morphology of a large-scale mag-

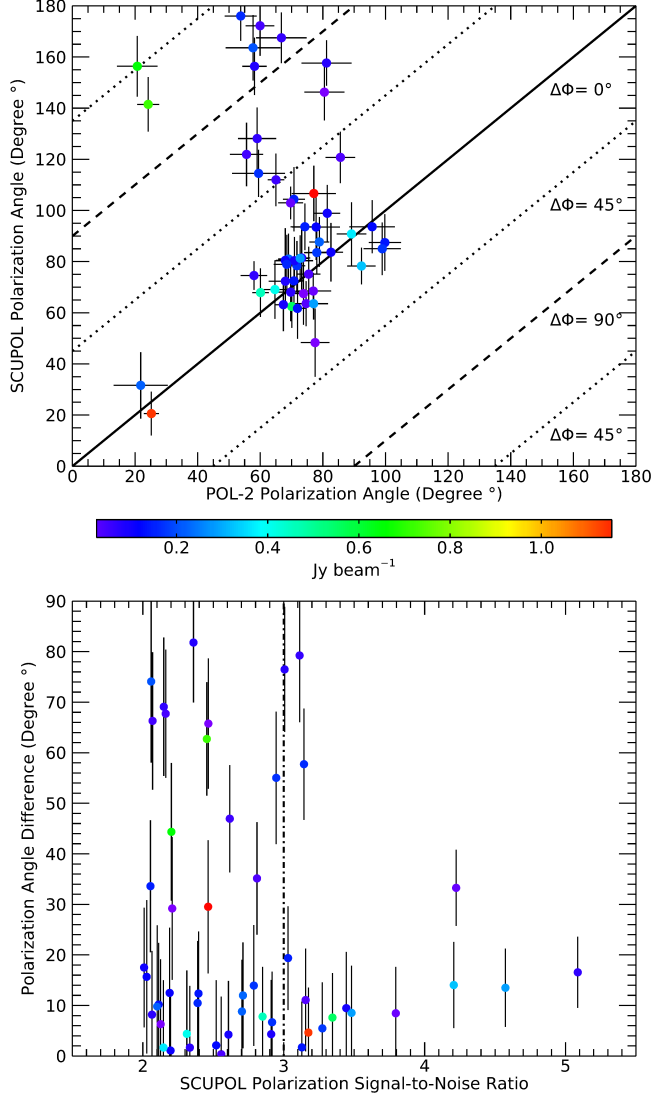


Figure 6. *Top:* Comparison of polarization angles for the 52 pairs of spatially overlapping POL-2 and SCUPOL vectors plotted in Figure 4. The plain line follows the 1:1 correspondence, and the dotted and dashed lines respectively trace differences of a 45 degrees and 90 degrees in polarization angle. *Bottom:* Difference of polarization angle between each pair of POL-2 and SCUPOL vector ($\Delta\Phi = |\Phi_{\text{SCUPOL}} - \Phi_{\text{POL-2}}|$) as a function of the signal-to-noise ratio (SNR) of the polarization fraction measured with SCUPOL ($P_{\text{SCUPOL}}/\sigma P_{\text{SCUPOL}}$). The vertical dashed line indicates a SNR of 3. In both panels, the color scale indicates the Stokes I intensity of the POL-2 vector associated with each point.

netic field. Since polarization vectors are expected to trace the plane-of-sky component of the magnetic field, we can infer the strength of this component by measuring the dispersion of polarization angles relative to the large-scale field orientation. This technique, however,

also requires the velocity dispersion and the density of the gas in the cloud to be known beforehand.

According to Crutcher et al. (2004), the DCF equation for the plane-of-sky magnetic field strength B_{pos} can be written as:

$$B_{\text{pos}} = A \sqrt{4\pi\rho} \frac{\delta V}{\delta\Phi}, \quad (6)$$

where ρ is the density, δV is the velocity dispersion of the gas in the cloud, $\delta\Phi$ is the dispersion of polarization angles (in radians), and A is a correction factor usually assumed to be ~ 0.5 . The correction factor A is included to account for the three-dimensional nature of the interplay between turbulence and magnetism (e.g., Ostriker et al. 2001). There is, however, a caveat to Equation 6, namely that it cannot intrinsically account for changes in the large-scale field morphology. As a consequence, the technique from Crutcher et al. (2004) was modified by Pattle et al. (2017) to take large-scale variations in field morphology into account when calculating the magnetic field strength in Orion A.

Specifically, Pattle et al. (2017) calculate the dispersion $\delta\Phi$ of polarization angles in Equation 6 with an unsharp-masking technique. First, the large-scale component of the field is found by smoothing the map of polarization angles using 3×3 -pixels boxes. This smoothed map is then subtracted from the original to obtain a map of the residual polarization angles. Finally, the dispersion $\delta\Phi$ is obtained from the mean value of the residual angles fitting a specific set of conditions. This approach therefore cancels the contribution of a changing field morphology to the dispersion of polarization angles at scales larger than the smoothed mean-field map.

In our work, we instead apply the improved DCF method developed by Hildebrand et al. (2009) and Houde et al. (2009), which was also adapted for polarimetric data obtained by interferometers such as the SMA and CARMA (Houde et al. 2011, 2016). This technique avoids the problem of spatial changes in field morphology by using an angular dispersion function (sometimes called structure function) rather than the dispersion of polarization angles around a mean value. Furthermore, the angular dispersion technique from Houde et al. (2009) was independently tested using both R-band (e.g., Franco et al. 2010) and submillimeter (e.g., Ching et al. 2017) polarimetric observations to characterize the magnetic and turbulent properties of star-forming regions.

This angular dispersion function is calculated by taking the angular difference between every pair of polarization vectors in a given map as a function of the distance between them. This technique effectively traces the ratio between turbulent and magnetic energies, which can

then be fitted without any prior assumptions on the turbulence in the cloud or the morphology of the large-scale field (Hildebrand et al. 2009). As before, this analysis can be used to estimate the strength of the plane-of-sky magnetic field component if the density and velocity dispersion of the cloud are known. Additionally, it can be used to measure the effect of integrating turbulent cells along the line-of-sight within a telescope beam, effectively constraining the theoretical factor A included in Equation 6 (Houde et al. 2009).

We first need to define the relevant quantities for the dispersion analysis presented in this paper. The difference in polarization angle between two vectors as a function of distance ℓ is defined as: $\Delta\Phi(\ell) \equiv \Phi(\mathbf{x}) - \Phi(\mathbf{x} + \ell)$, where $\Phi(\mathbf{x})$ is the angle Φ of the polarization vector found at a position \mathbf{x} in the map and ℓ is the angular displacement between two vectors. With this quantity, we can define the angular dispersion function as formulated by Houde et al. (2009):

$$1 - \langle \cos[\Delta\Phi(\ell)] \rangle, \quad (7)$$

where $\langle \dots \rangle$ is the average over every pair of vectors separated by a distance ℓ . Since Equation 7 is essentially a measure of the mean difference in polarization angles as a function of distance, it is accurate to describe it as an angular dispersion function.

The magnetic field $\mathbf{B}(\mathbf{x})$ in the cloud at a position \mathbf{x} can be written as a combination of a large-scale (or ordered) component $\mathbf{B}_o(\mathbf{x})$ and a turbulent component $\mathbf{B}_t(\mathbf{x})$, i.e., $\mathbf{B}(\mathbf{x}) = \mathbf{B}_o(\mathbf{x}) + \mathbf{B}_t(\mathbf{x})$. Furthermore, we define the ratio between the average energy of the turbulent component to that of the large-scale component as $\langle B_t^2 \rangle / \langle B_o^2 \rangle$ and the ratio between the average energy of the turbulent component to that of the total magnetic field as $\langle B_t^2 \rangle / \langle B^2 \rangle$. Both quantities can be obtained from fitting the angular dispersion function.

To relate the magnetic fields and turbulence, we also need to define the turbulent properties of the cloud. Specifically, we require the number N of independent magnetic turbulent cells observed for a column of dust along the line-of-sight and within a telescope beam from:

$$N = \Delta' \frac{(\delta^2 + 2W^2)}{\sqrt{2\pi} \delta^3}, \quad (8)$$

where δ is the turbulent correlation length scale of the magnetic field, W is the radius of the circular telescope beam (specifically, $\text{FWHM} = 2\sqrt{2\ln 2}W$), and Δ' is the effective thickness of the cloud (see Equation 52 in Houde et al. 2009). The turbulent correlation length scale δ can be understood as the typical size of a magnetized turbulent cell in the cloud. In this specific case, the turbulence is supposedly isotropic and the turbulent

correlation length scale δ is assumed to be smaller than the thickness Δ' of the cloud.

If the physical depth of the cloud is not known beforehand, the effective thickness Δ' can be estimated from the autocorrelation function of the integrated polarized intensity across the cloud (see Equation 51 in Houde et al. 2009). This autocorrelation function is defined as:

$$\langle I_P^2(\ell) \rangle \equiv \langle I_P(\mathbf{x}) I_P(\mathbf{x} + \ell) \rangle, \quad (9)$$

from which we use the width at half-maximum to evaluate Δ' . This approach, however, assumes that the spatial distribution of polarized dust emission on the plane-of-sky is an adequate probe of the cloud's properties along the line-of-sight, which we believe to be reasonable in the case of dense molecular clouds.

The detailed derivations given by Hildebrand et al. (2009) and Houde et al. (2009) show that the relationship between the angular dispersion function and the magnetic and turbulent properties of a molecular cloud can be expressed by the following equation:

$$1 - \langle \cos[\Delta\Phi(\ell)] \rangle \simeq \frac{1}{N} \frac{\langle B_t^2 \rangle}{\langle B_o^2 \rangle} - b^2(\ell) + a\ell^2, \quad (10)$$

where a is the first Taylor coefficient of the ordered autocorrelation function, and $b^2(\ell)$ is the autocorrelated turbulent component of the dispersion function (see Equations 53 and 55 in Houde et al. 2009). Specifically, the Taylor coefficient a is related to the large-scale structure of the magnetic field. Additionally, we can write this autocorrelated turbulent component as:

$$b^2(\ell) = \frac{1}{N} \frac{\langle B_t^2 \rangle}{\langle B_o^2 \rangle} e^{-\ell^2/2(\delta^2+2W^2)}. \quad (11)$$

Since the beam radius W and the effective cloud thickness Δ' can be considered as known quantities, we only need to fit three parameters to the angular dispersion function: the ratio of turbulent energy to large-scale magnetic energy $\langle B_t^2 \rangle / \langle B_o^2 \rangle$, the turbulent correlation length scale δ of the magnetic field, and the first Taylor coefficient a of the ordered autocorrelation function.

Finally, Houde et al. (2009) rewrote the DCF equation (see Equation 6) for the plane-of-sky strength of the magnetic field to calculate it directly from the ratio of turbulent energy to total magnetic energy $\langle B_t^2 \rangle / \langle B^2 \rangle$ in the cloud. This new formulation of the DCF equation can be written as:

$$B_{\text{pos}} \simeq \sqrt{4\pi\rho} \delta V \left[\frac{\langle B_t^2 \rangle}{\langle B^2 \rangle} \right]^{-1/2}, \quad (12)$$

where as previously ρ is the density and δV is the one-dimensional velocity dispersion for the gas (see

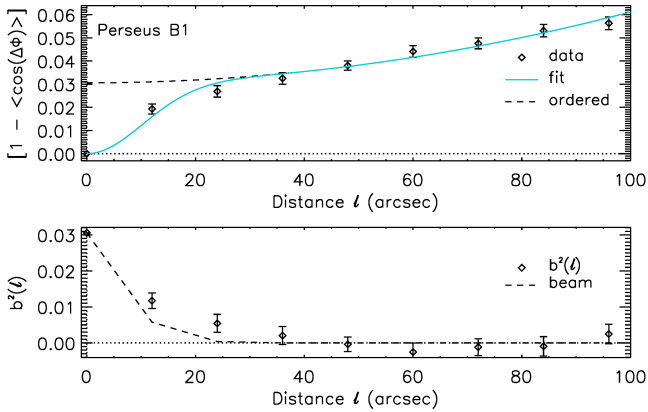


Figure 7. Dispersion of polarization angles for POL-2 observations of Perseus B1. *Top:* The angular dispersion function $[1 - \cos(\Delta\Phi)]$ as a function of the distance ℓ . The fit of Equation 10 to the data is shown with (blue solid line) and without (black dashed line) including the autocorrelation function $b^2(\ell)$ defined in Equation 11. *Bottom:* Signal-integrated turbulence autocorrelation function $b^2(\ell)$ as a function of distance ℓ . The black dashed line shows the contribution of the telescope beam alone.

Equation 57 in Houde et al. 2009 and Equation 26 in Houde et al. 2016). The gas density ρ takes the form $\rho = \mu m_H n(H_2)$, where $\mu = 2.8$ is the mean molecular weight of the gas (Kauffmann et al. 2008), m_H is the mass of an hydrogen atom, and $n(H_2)$ is the number density of hydrogen molecules in the cloud.

Once the strength of the plane-of-sky component of the magnetic field has been calculated with Equation 12, it becomes possible to evaluate the magnetic critical ratio λ_c of the studied molecular cloud (Crutcher et al. 2004). The critical ratio λ_c can be estimated from the plane-of-sky amplitude of the magnetic field with the following equation:

$$\lambda_c \simeq 7.6 \times 10^{-21} \frac{N(H_2)}{B_{\text{pos}}}, \quad (13)$$

where $N(H_2)$ is the typical column density of molecular hydrogen in the cloud. If $\lambda_c < 1$, then the molecular cloud is magnetically subcritical and the magnetic field is sufficiently strong to stop its gravitational collapse. If $\lambda_c > 1$, the cloud is instead magnetically supercritical and the magnetic field alone cannot support the cloud against its self-gravity.

4.2. Cloud Characteristics and Magnetic Field Strength in Perseus B1

Following Section 4.1, we determine the angular dispersion function from the POL-2 data of Perseus B1. We include in this analysis all the POL-2 polarization vectors found in a 240 arcsec-wide square centered on

the position (03^h 33^m 20^s.45, +31° 07' 50".16), as illustrated in the right panel of Figure 1. This region covers most of the embedded young stellar objects in the densest parts of Perseus B1. The resulting angular dispersion function is shown in the top panel of Figure 7 as a function the distance ℓ in bins of 12 arcsec. The observed steady increase of this function with ℓ at small spatial scales (0.01 to 1.0 pc) is also a behavior seen in other studies using this technique (e.g., Houde et al. 2009, 2016; Franco et al. 2010; Ching et al. 2017; Chuss et al. 2019).

The angular dispersion function was fitted with Equation 10 to obtain δ and $\langle B_t^2 \rangle / \langle B_o^2 \rangle$ using an effective cloud depth Δ' of 84 arcsec, and a beam radius W of 6.2 arcsec (or a FWHM of 14.6 arcsec) at 850 μ m. The reduced chi-squared value for this fit is $\chi_r^2 = 1.5$. The results of the fit to the angular dispersion, including $\langle B_t^2 \rangle / \langle B^2 \rangle$, are given in Table 1. Additionally, the resulting turbulent autocorrelation function $b^2(\ell)$ is shown on the bottom panel of Figure 7.

At a distance of 295 pc (Ortiz-León et al. 2018), the effective cloud depth Δ' of 84 arcsec in B1 represents a physical depth of ~ 0.1 pc. While this effective cloud depth $\Delta' \sim 0.1$ pc was derived independently from the autocorrelation function of the polarized intensity I_P (see Section 4.1), it is nonetheless comparable to the typical width of dense filaments in star-forming regions (e.g., Arzoumanian et al. 2011; André et al. 2014; Koch & Rosolowsky 2015; André et al. 2016). For reference, the square region shown in the right panel of Figure 1 has a width ~ 0.4 pc (~ 270 arcsec).

The exact distance to the Perseus molecular cloud, and to B1 in particular, is still subject to some ambiguity. Indeed, different methods provide a wide range of values from 235 pc (22 GHz water maser parallaxes; Hirota et al. 2008, 2011) to 315 pc (photometric reddening; Schlafly et al. 2014). Furthermore, Schlafly et al. (2014) found a gradient of distances from the western (260 pc) to the eastern (315 pc) parts of the Perseus molecular cloud complex. However, recent parallaxes measurements with the *Gaia* space telescope instead suggest a smaller range of distances between NGC 1333 (295 pc) and IC 348 (320 pc) (Ortiz-León et al. 2018). According to these *Gaia* results, the distance to B1 is similar to that of NGC 1333 at 295 pc. This distance to B1 assumes that the young stellar objects used for these parallaxes measurements provide a good estimate of the clump's true position along the line-of-sight.

Perseus B1 was mapped in emission from several NH₃ inversion transitions at ~ 24 GHz by GAS (the first data release of the survey was presented by Friesen et al. 2017). NH₃ is a commonly-used selective tracer of mod-

erately dense gas ($n \gtrsim$ a few 10^3 cm $^{-3}$; Shirley 2015). The NH₃ (1,1) emission closely follows the intensity detected with POL-2 across the cloud (GAS Consortium, in prep.). The velocity dispersion of the gas along each line-of-sight was obtained through simultaneous modeling of hyperfine structure of the detected NH₃ (1,1) and (2,2) inversion line emission. Assuming that the (1,1) and (2,2) lines share the same line-of-sight velocity, velocity dispersion, and excitation temperature, the analysis produces maps of the aforementioned parameters along with the gas kinetic temperature, and the total column density of NH₃. Further details of the modeling are given in Friesen et al. (2017).

For the region delimited by the square in the right panel of Figure 1, we find an average velocity dispersion $\delta V = 0.29$ km s $^{-1}$, with a standard deviation $\sigma_{\delta V} = 0.11$ km s $^{-1}$. The uncertainties for individual line width measurements are typically < 0.05 km s $^{-1}$. We therefore use the velocity dispersion $\delta V = (2.9 \pm 1.1) \times 10^4$ cm s $^{-1}$ to calculate the plane-of-sky amplitude of the magnetic field with Equation 12.

The number density $n(\text{H}_2)$ of the gas in Perseus B1 is also calculated from the same GAS NH₃ data (Friesen et al. 2017; GAS Consortium, in prep.). Specifically, we follow the relation described by Ho & Townes (1983) between density, excitation temperature, and gas kinetic temperature to estimate the number density $n(\text{H}_2)$ in B1, assuming the NH₃ emission in B1 can be approximated by a two-level system. First, for the denser regions associated with polarized emission, we find a mean gas temperature of 11.6 K with a standard deviation of 1.2 K, and a mean excitation temperature of 6.5 K with a standard deviation of 0.4 K. Using these temperatures, we calculate a mean density $n(\text{H}_2) = (1.5 \pm 0.3) \times 10^5$ cm $^{-3}$. If the typical depth of the dense material in B1 is indeed ~ 0.1 pc, we then find a column density $N(\text{H}_2) = (4.7 \pm 0.9) \times 10^{22}$ cm $^{-2}$ in agreement with the values obtained from fitting far-infrared and submillimeter measurements of dust thermal emission (Sadavoy et al. 2013; Chen et al. 2016). Finally, assuming a molecular weight $\mu = 2.8$ (Kauffmann et al. 2008), we derive an average gas density $\rho = (7.0 \pm 1.4) \times 10^{-19}$ g cm $^{-3}$.

The ratio $\langle B_t^2 \rangle / \langle B^2 \rangle$ of turbulent-to-total magnetic energy given in Table 1 can be used to calculate the plane-of-sky strength of the magnetic field in Perseus B1 using Equation 12. Combined with the values given previously for the density ρ and velocity dispersion δV , we calculate the plane-of-sky strength of the magnetic field in Perseus B1 to be 120 ± 60 μG .

We compare the plane-of-sky strength of the magnetic field derived from the angular dispersion analy-

sis (Houde et al. 2009) with the one obtained from the classical DCF method (Crutcher et al. 2004). First, we fit a Gaussian curve to the histogram of POL-2 polarization angles shown in the top panel of Figure 5 and find a dispersion $\delta\Phi_{\text{obs}} = 0.213$ radians (12.2°). We then evaluate the dispersion $\delta\Phi_{\text{err}}$ due to instrumental errors using the mean uncertainty in polarization angle of 0.099 radians (5.7°) given in Section 3.2. This allows us to calculate the intrinsic angular dispersion $\delta\Phi = \sqrt{\delta\Phi_{\text{obs}}^2 - \delta\Phi_{\text{err}}^2} = 0.188$ radians (10.8°). We then use Equation 6, assuming a correction factor $A = 0.5$ (e.g., Pattle et al. 2017; Soam et al. 2018; Kwon et al. 2018), to derive a plane-of-sky magnetic field amplitude $B_{\text{pos}} \sim 230$ μG . This larger value for B_{pos} suggests that a more appropriate correction factor for B1 would be $A \sim 0.25$. However, this derived field strength of 230 μG could even be a lower limit (in the context of the classical DCF method) since the polarization vectors around B1-c are also included in the Gaussian fit, and so the appropriate correction factor to use would in fact be $A \lesssim 0.25$.

With the magnetic field amplitude $B_{\text{pos}} = 120 \pm 60$ μG we have obtained from the angular dispersion analysis, it becomes possible to estimate the criticality criterion λ_c of Perseus B1 with Equation 13. Using the hydrogen column density $N(\text{H}_2) = (4.7 \pm 0.9) \times 10^{22}$ cm $^{-2}$ derived previously, we find $\lambda_c = 3.0 \pm 1.5$. Since $\lambda_c > 1$, Perseus B1 is a magnetically supercritical molecular cloud, i.e., magnetic pressure alone cannot support the cloud against gravity.

Perseus B1 is among a few molecular clouds with a detection of OH Zeeman splitting, and thus a measurement of its magnetic field's line-of-sight component. With observations of the OH lines at 1665 MHz and 1667 MHz using the Arecibo telescope and a beam width of 2.9 arcmin, Goodman et al. (1989) found a line-of-sight amplitude of 27 ± 4 μG for the magnetic field towards IRAS 03301+3057 (B1-a). While this value might have been overestimated relative to the line-of-sight amplitude of the magnetic field at large scales (Crutcher et al. 1993; Matthews & Wilson 2002), it nonetheless supports the idea that the orientation of the magnetic field in B1 might be mostly parallel to the plane of the sky (i.e., an inclination $\theta < 15^\circ$ relative to the plane of the sky).

5. DISCUSSION

5.1. Morphology of the Magnetic Field

The magnetic field in Perseus B1, as shown in the right panel of Figure 1, is seen to run roughly North-South (or $\sim 165^\circ$ East of North) across the whole region, including SMM3. The orientation of the vectors seen in Figure 1 (right) towards the bulk of the cloud (between B1-b N/S

Table 1. Derived magnetic and turbulent properties, and other related parameters in Perseus B1

Parameter	Value	Description
δ	5.0 ± 2.5 arcsec	Turbulent correlation length scale
N	27.3 ± 0.3	Number of beam-integrated turbulent cells along the line-of-sight
$\langle B_t^2 \rangle / \langle B_o^2 \rangle$	0.9 ± 1.1	Turbulent-to-ordered magnetic energy ratio
$\langle B_t^2 \rangle / \langle B^2 \rangle$	0.5 ± 0.3	Turbulent-to-total magnetic energy ratio
a	$(2.4 \pm 0.2) \times 10^{-6}$ arcsec $^{-2}$	First Taylor coefficient of the ordered auto-correlation function
δV	$(2.9 \pm 1.1) \times 10^4$ cm s $^{-1}$	Velocity dispersion of the gas along the line-of-sight ^a
$n(\text{H}_2)$	$(1.5 \pm 0.3) \times 10^5$ cm $^{-3}$	Mean number density of the gas ^a
$N(\text{H}_2)$	$(4.7 \pm 0.9) \times 10^{22}$ cm $^{-2}$	Estimated column density for a cloud depth of ~ 0.1 pc
ρ	$(7.0 \pm 1.4) \times 10^{-19}$ g cm $^{-3}$	Estimated density of the gas for a molecular weight $\mu = 2.8$
B_{pos}	120 ± 60 μG	Plane-of-sky amplitude of the magnetic field
λ_c	3.0 ± 1.5	Criticality ratio ^b

^a Friesen et al. 2017; GAS Consortium, in prep.

^b Crutcher et al. 2004

and SMM3) can be explained if B1 is part of a dense, slightly flattened cylindrical filament threaded perpendicularly by a large-scale magnetic field and viewed at an inclined angle to the line-of-sight (Tomisaka 2015). While it may not be clear from Figure 1 alone, Perseus B1 is indeed part of a large filamentary structure extending towards the South-Western part of the map (Chen et al. 2016). Furthermore, magnetic field lines perpendicular to large-scale filaments have been hypothesized to funnel low density material into the striations (or sub-filaments) observed with *Herschel* in and around molecular clouds (André et al. 2014). Alternatively, if the cloud is collapsing gravitationally, then the apparent curving of the field lines West of SMM3 could be the sign of an emergent hourglass morphology (e.g., Girart et al. 2006).

The largest discrepancy in the morphology of the large-scale magnetic field is seen towards the protostellar core B1-c, which is the source of a powerful molecular outflow viewed almost edge-on (Matthews et al. 2006). Indeed, the field turns more towards an East-West direction (or $\sim 120^\circ$ East of North) in the vicinity of B1-c, where it seems instead better aligned with the orientation of the protostellar outflow traced by the ^{12}CO J=3-2 integrated intensity contour. In fact, the plane-of-sky component of the magnetic field towards B1-c is nearly parallel to the orientation of the outflow at 125° . In contrast, the local magnetic field direction is relatively well aligned with the mean field orientation in Perseus B1 ($\sim 165^\circ$) at the locations of the candidate

first hydrostatic cores, and potentially less evolved, B1-bN ($\sim 155^\circ$) and B1-bS ($\sim 165^\circ$) objects (Pezzuto et al. 2012; Gerin et al. 2017), as well as at the previously identified young stellar objects associated with the submillimeter sources B1-a ($\sim 159^\circ$) and SMM3 ($\sim 158^\circ$), and to a lesser extent B1-d ($\sim 10^\circ$) and HH 789 ($\sim 180^\circ$) (Bally et al. 2008). This directional variation suggests that the magnetic field morphology is well ordered at large scales, but is potentially locally modified by the motion of the gas at smaller scales.

Perhaps the magnetic field orientation at B1-c originally followed the large-scale field of the molecular cloud, but was misaligned with the angular momentum of the initial prestellar core. As the core evolved, the magnetic field lines may have been “dragged” into a modified hourglass configuration (e.g., Kataoka et al. 2012). However, although hourglass structures have been seen toward some protostellar cores (e.g., Girart et al. 2006; Hull et al. 2017a), an alignment between magnetic field and outflow orientations does not appear to be a common occurrence (Hull et al. 2014).

Alternatively, the orientation of the magnetic field at B1-c could be explained by more complex field models which have been shown to produce comparable polarization patterns (Franzmann & Fiege 2017). Indeed, recent ALMA observations of the protostellar core Seremb 8 in Serpens Main suggest that the magnetic field of that object, which is similarly misaligned with the large-scale field of the rest of the molecular cloud in which it is embedded, may not possess an hourglass morphol-

ogy at all (Hull et al. 2017b). However, the protostellar core Serpens SMM1 (also in Serpens Main) nevertheless shows evidence of having an hourglass field morphology while still being misaligned with the magnetic field at larger scales (Hull et al. 2017a). It would therefore be premature to assume that an observed misalignment in magnetic field orientations between core and cloud scales necessarily implies the absence of an hourglass field morphology.

Another peculiar property of B1-c is the orientation of the few polarization vectors found East from the protostellar core and along its outflow, as traced by the ^{12}CO $J=3-2$ contour in Figure 1. The inferred magnetic field orientation from the vectors found directly in the outflow's path ($\sim 160^\circ$) is in better agreement with the large-scale field in B1 ($\sim 165^\circ$) than with the field orientation towards B1-c itself ($\sim 120^\circ$). Magnetic field orientations that are nearly perpendicular to outflows at large scales are not expected from ideal hourglass field morphologies.

An alternative explanation would be that elongated dust grains found in the vicinity of the outflow are aligned mechanically by the flow of gas instead of radiatively. In this case, the polarization vectors would be parallel (and the inferred magnetic field orientation perpendicular) to the outflow orientation, regardless of the field morphology (Gold 1952; Lazarian 1997, 2007), as is seen. This last scenario, however, has been shown to be unlikely even in the case of explosives outflows such as in Orion BN/KL (Tang et al. 2010).

Indeed, the original mechanical alignment proposed by Gold (1952) requires supersonic flows to be efficient, and it is particularly inefficient for suprathermally rotating grains (see Lazarian 1997, Das & Weingartner 2016). Thus, although its polarization pattern seems to be consistent with the observed polarization map, it is rather difficult to explain the high polarization degree (~ 15 per cent) shown in Figure 1. On the other hand, the Mechanical Torque (MAT) alignment mechanism proposed by Lazarian & Hoang (2007b) and numerically demonstrated by Hoang et al. (2018) predicts that the gas flow can efficiently align grains with the magnetic field. Specifically, the MAT mechanism predicts that the long-axis of the grains will be perpendicular either to the magnetic field or the gas flow. Therefore, the polarization vectors found along the outflow's lobes may reveal that the magnetic field in the flow is not much different from the large-scale magnetic field in the rest of the molecular cloud.

Finally, there is the possibility that we are mainly measuring the polarization from dust grains found in the cavity walls of the B1-c outflow. Indeed, it has

been suggested that strong irradiation of outflow cavity walls can enhance the polarized emission of the associated dust grains through radiative torques (e.g., Maury et al. 2018). This scenario is supported by ALMA observations of B1-c (or Per-emb-29) (Cox et al. 2018) which provide evidence for significantly improved grain alignment (with $P > 5$ per cent) along outflow cavities near the protostar. Although previous ALMA studies have shown that the magnetic field along comparable outflow cavities tend to be parallel to the outflow orientation (Hull et al. 2017a; Maury et al. 2018; Cox et al. 2018) instead of perpendicular as observed eastward from B1-c in Figure 1, their spatial resolutions were much smaller (140 au, 60 au, and 100 au respectively) than our resolution of ~ 3500 au. It could be that the dust grains with potentially enhanced polarized emission farther along the outflow cavity are instead tracing the large-scale field in the cloud, which would fit with the twisted field picture from Kataoka et al. (2012) where the polarization signature becomes less affected by the outflow the farther away you look from the central source.

5.2. Magnetic and Turbulent Properties

In Section 4.2, we derived the turbulent and magnetic properties of Perseus B1 from the angular dispersion analysis described by Houde et al. (2009) (see Figure 7). Specifically, we obtain a ratio of turbulent-to-total magnetic energy $\langle B_t^2 \rangle / \langle B^2 \rangle = 0.5 \pm 0.3$, which indicates that a large part of the magnetic energy in the cloud is found in the form of magnetized turbulence. This is larger than the ratio $\langle B_t^2 \rangle / \langle B^2 \rangle \sim 0.4$ found by Levrier et al. (2018) for the galactic magnetic field using Planck data. As a comparison, a previous study utilizing the angular dispersion analysis presented in Section 4.1 found ratios of turbulent-to-total magnetic energy $\langle B_t^2 \rangle / \langle B^2 \rangle$ of, respectively, 0.6, 0.7 and 0.7 for the high mass star-forming regions W3(OH), W3 Main and DR21(OH) (Houde et al. 2016).

Since the ionized and neutral components of the gas in molecular clouds are typically well coupled, this magnetized turbulence is expected to be indistinguishable from the turbulence in the neutral gas as long as ambipolar diffusion remains negligible (e.g., Krumholz 2014). Furthermore, the relatively large turbulent component of the magnetic field in B1 could be explained by the presence of at least five young stellar objects with confirmed molecular outflows (B1-a, B1-bS, B1-c, B1-d, and HH 789) in the main body of the cloud (Hatchell & Dunham 2009). Indeed, such outflows are among the most probable drivers of turbulence in molecular clouds (Bally et al. 2008). However, the signature of this protostellar feedback on the velocity dispersion of NH_3 does

not appear to be as pronounced in B1 (GAS Consortium, in prep.) as it is in the more compact B59 in the Pipe nebula (see Figure 9 in Redaelli et al. 2017), but a more detailed coherence analysis will be required to adequately investigate this effect.

The turbulent cells in B1 have a correlation length δ of 5.0 ± 2.5 arcsec, which for a distance of 295 pc represents a physical length of 1475 au. From Equation 8, we estimate that there are typically ~ 30 turbulent cells probed by the telescope’s beam along the depth of the cloud (0.1 pc). The number of turbulent cells along the line-of-sight could potentially be greater in higher density regions, such as towards pre-stellar cores. This larger number would explain the observed depolarization effect seen in Figure 2 (top) as the Stokes I intensity increases, which can be roughly understood as an increase in the dust column density. Indeed, an increased number of turbulent cells is expected to randomize dust orientations along the line-of-sight, and thus decrease the measured fraction of polarization P . Additionally, and perhaps counter-intuitively, numerical simulations by Cho & Yoo (2016) have also shown that the averaging of a high number of turbulent cells along the line-of-sight could preserve the appearance of a well-ordered field morphology at large scales, which is an effect initially proposed by Jones et al. (1992).

In Section 4.2, we also find a plane-of-sky amplitude $B_{\text{pos}} = 120 \pm 60 \mu\text{G}$ for the magnetic field, and a criticality criterion $\lambda_c = 3.0 \pm 1.5$. Although this magnetic field amplitude is relatively weak when compared to the fields found in high mass star-forming regions such as Orion A (where $B_{\text{pos}} \gtrsim 1.0 \text{ mG}$) (e.g., Houde et al. 2009; Pattle et al. 2017) or in hub-filament structures such as IC 5146 (with $B_{\text{pos}} \sim 0.5 \text{ mG}$) (e.g., Wang et al. 2018), it is either comparable to or larger than the field strengths ($B_{\text{pos}} \lesssim 100 \mu\text{G}$) typically found in low-mass prestellar cores (e.g., Crutcher et al. 2004; Kirk et al. 2006; Liu et al. 2019). Above all, these results indicate that Perseus B1 is a supercritical molecular cloud (i.e., magnetic pressure alone cannot support the cloud against gravity). The criticality criterion λ_c defined by Equation 13, however, may be overestimated due to geometric effects. Indeed, Crutcher et al. (2004) find that, on average, the effective criticality criterion is $\bar{\lambda}_c \approx \lambda_c/3$. In the case of B1, this adjustment would lead to $\bar{\lambda}_c \approx 1.0$, which is the theoretical limit at which the cloud would be subcritical.

Since the inclination of the magnetic field in B1 can be calculated using published Zeeman line splitting measurements (see Section 4.2), we can better estimate the effect of geometry on the criticality criterion $\bar{\lambda}_c$. Assuming that the line-of-sight component obtained by Good-

man et al. (1989) ($27 \pm 4 \mu\text{G}$) is not an overestimation at large scales, we find an inclination $\theta = 12^\circ$ relative to the plane of the sky and an amplitude $B_{\text{tot}} \approx 125 \mu\text{G}$ for the total magnetic field when combined with the plane-of-sky amplitude $B_{\text{pos}} = 120 \pm 60 \mu\text{G}$ found in Section 4.2. If the cloud can also be approximated as a mostly prolate filament with a cylindrical symmetry, which is a reasonable assumption for a relatively weak magnetic field in a dense filament, then we get $\bar{\lambda}_c \approx \lambda_c$. We therefore find it likely that Perseus B1 is indeed supercritical by a factor ~ 3 , although we cannot rule out if a combination of magnetic pressure and turbulence would be sufficient to significantly slow down the fall of additional material onto the central clump.

5.3. Polarization Fraction and Grain Alignment

Fundamentally, the fraction P of polarization can be understood as the alignment efficiency of a mixture of dust grains in the interstellar medium. Even though this fraction P can be affected by purely environmental factors such as the number of integrated turbulent cells along the line-of-sight and complex magnetic field geometries, or even instrumental factors such as molecular contamination (see Appendix A), it is intrinsically linked to the models of grain alignment.

Specifically, the contribution to the continuum emission of different grain sizes and compositions in the dust mixture could explain the apparent dependence of P on the wavelength at far-infrared and submillimeter wavelengths (Vaillancourt & Matthews 2012). For example, grain growth in cold high density regions may lead to very large dust grains, with sizes $a \gtrsim 1.0 \mu\text{m}$ (e.g., Paganini et al. 2010), which align less efficiently through radiative torques than the typical grains ($a \sim 0.1 \mu\text{m}$) found in molecular clouds (Hoang & Lazarian 2009). This scenario could potentially explain the apparent drop in polarization fraction P seen in Figure 3 above a visual extinction $A_V > 200$ mag, as well as towards B1-c, since there is significant evidence for grain growth across Perseus B1 (Sadavoy et al. 2013; Chen et al. 2016).

Furthermore, since the RAT theory of grain alignment depends on the stellar radiation field incident on the grains, the alignment efficiency is expected to be smaller towards regions with high dust opacities (e.g., dense prestellar cores) (Andersson et al. 2015). This effect would potentially explain the apparent minimum P of ~ 1 per cent seen both in Figure 2 (top) and by Matthews & Wilson (2002) for the highest opacity regions of the cloud, which in the case of Perseus B1 are associated with embedded young stellar objects such as the first hydrostatic core candidates B1-b N/S (see Fig-

ure 1). This alignment efficiency, however, is expected to improve again if there is a significant source of radiation, such as a protostar, within the core itself. Such a scenario would explain the shallower than expected power index $\beta \sim -0.5$ given in Section 3.2 for the relation between the polarization fraction P and the visual extinction A_V in Perseus B1.

Nevertheless, B1-c, which is known to be a bright and warm protostellar core (Sadavoy et al. 2013), also has among the lowest polarization fractions measured by POL-2 for B1. This behavior suggests that we may not be resolving the improved grain alignment efficiency seen by ALMA near the protostar (Cox et al. 2018). Indeed, Jones et al. (2016) previously observed such an effect when comparing single-dish and interferometric polarization data of the protostellar core G034.43+00.24 MM1. Alternatively, it could be that factors other than alignment efficiency need to be taken into account to explain the polarization towards this object.

As an example, previous studies have found an inverse correlation between the polarization fraction P and the local dispersion of magnetic field orientations at several scales in molecular clouds (Planck Collaboration et al. 2015a,b; Fissel et al. 2016; Koch et al. 2018). Such a measure towards B1-c would support the hypothesis of a complex but unresolved polarization structure, and higher resolution observations using interferometric facilities would provide further evidence to confirm or infirm this scenario. However, while there exist ALMA data of the linear polarization towards B1-c, only the most highly polarized emission is likely to have been recovered due to the short integration time (8 minutes) of these observations (Cox et al. 2018). A deeper ALMA polarization map of B1-c might therefore reveal a more complex magnetic field structure comparable to those observed in similar protostellar cores (e.g., Hull et al. 2017b,a; Maury et al. 2018).

6. CONCLUSION

We have observed the 850 μm linear polarization towards the B1 clump in the Perseus molecular cloud complex using the POL-2 polarimeter as part of the BISTRO survey at the JCMT. We have also compared the resulting polarization map with previously published SCUPOL observations of B1 from Matthews et al. (2009) to illustrate the improvements brought by the increased sensitivity and reliability of POL-2 over its predecessor. From the POL-2 observations, we have inferred the plane-of-sky morphology of the magnetic field in Perseus B1 by rotating the 850 μm polarization vectors by 90° assuming the dust grains are aligned by radiative torques (e.g., Andersson et al. 2015). The plane-

of-sky component of the magnetic field in most of the cloud is orientated in a North-South direction (or $\sim 165^\circ$ East of North), except towards the protostellar core B1-c where it turns more East-West in better agreement with the orientation of its associated molecular outflow.

We have also plotted the polarization fraction P and the de-biased polarized intensity I_P as a function of the Stokes I total intensity. Specifically, we have fitted a power-law to the relationship between P and I , and we find a power index $\alpha \sim -0.9$ in agreement with other BISTRO studies. There exists a clear trend in Perseus B1 of decreasing polarization fraction P as a function of increasing Stokes I , although the polarized intensity I_P itself appears to increase steadily. Such a behavior is likely linked to depolarization effects towards higher density regions, such as a complex field geometry, a low efficiency of grain alignment, or an increased number of turbulent cells along the line-of-sight.

Similarly, we have plotted the polarization fraction P as a function of the visual extinction A_V in Perseus B1, and fitted a power-law between the two parameters. We find a power index $\beta \sim -0.5$, which is a shallower value than those previously found in starless cores with comparable extinction measurements ($A_V > 20$). This shallow power index $\beta \sim -0.5$ could therefore be explained by improved grain alignment due to the radiation from embedded young stellar objects in the cloud.

We have applied the angular dispersion analysis developed by Houde et al. (2009) to the POL-2 850 μm polarization map of Perseus B1. By fitting the angular dispersion function, we have measured a turbulent magnetic correlation length δ of 5.0 ± 2.5 arcsec, which for a distance of 295 pc represents a physical length of ~ 1500 au, and a turbulent-to-total magnetic energy ratio of 0.5 ± 0.3 inside the cloud. Such a large ratio indicates that a significant part, if not most, of the magnetic energy in the cloud is found in the form of magnetized turbulence. Additionally, using an effective cloud depth of ~ 0.1 pc, we have evaluated that there are typically ~ 30 beam-integrated turbulent cells along the line-of-sight across B1.

With an updated version of the Davis-Chandrasekhar-Fermi method, we have evaluated the plane-of-sky amplitude of the magnetic field in Perseus B1 to be $B_{\text{pos}} = 120 \pm 60$ μG . From this amplitude, we have estimated the magnetic criticality criterion in this cloud to be $\lambda_c = 3.0 \pm 1.5$. We also found with measurements of OH Zeeman line splitting that the orientation of the magnetic field is nearly parallel to the plane of the sky, and thus this criticality criterion is unlikely to be overestimated due to geometric effects. Perseus B1 is therefore a magnetically supercritical molecular cloud.

Finally, our findings show that the angular dispersion analysis presented by [Houde et al. \(2009\)](#) can be successfully applied to POL-2 observations of nearby star-forming regions. It will therefore be possible in future works to expand this analysis to a representative sample of molecular clouds in order to systematically quantify, and compare, their magnetic and turbulent properties. This illustrates how the BISTRO survey has the potential to provide us with unparalleled insight into the roles of magnetic fields and turbulence in the physical processes leading to the formation of stars and their planets.

ACKNOWLEDGEMENTS

We would like to thank the staff of the East Asian Observatory for their invaluable support in the completion of the BISTRO survey. We also wish to thank the people of Hawai'i for granting us access to the unique geographical site of the Maunakea observatory. Furthermore, we are grateful to the GAS Consortium for generously granting us access to their spectroscopic data. We also thank the anonymous reviewer for their helpful and detailed comments. Finally, we thank B.-G. Andersson, Kelvin Au, Jordan Guerra Aguilera, James Lane, Anna Ordog, Amélie Simon, Ian Stephens, and Julien Vandeportal for helpful discussions.

This research was conducted in part at the SOFIA Science Center, which is operated by the Universities Space Research Association under contract NNA17BF53C with the National Aeronautics and Space Administration.

The James Clerk Maxwell Telescope is operated by the East Asian Observatory on behalf of The National Astronomical Observatory of Japan; Academia Sinica Institute of Astronomy and Astrophysics; the Korea Astronomy and Space Science Institute; Center for Astro-

nomical Mega-Science (as well as the National Key R&D Program of China with No. 2017YFA0402700). Additional funding support is provided by the Science and Technology Facilities Council of the United Kingdom and participating universities in the United Kingdom and Canada.

SCUBA-2 and POL-2 were built through grants from the Canada Foundation for Innovation. This research used the facilities of the Canadian Astronomy Data Centre operated by the National Research Council of Canada with the support of the Canadian Space Agency. This research has also made use of the SIMBAD database and of NASA's Astrophysics Data System Bibliographic Services. The Starlink software ([Currie et al. 2014](#)) is currently supported by the East Asian Observatory.

Miju Kang was supported by Basic Science Research Program through the National Research Foundation of Korea (NRF) funded by the Ministry of Science, ICT & Future Planning (NRF-2015R1C1A1A01052160). Woojin Kwon was supported by Basic Science Research Program through the National Research Foundation of Korea (NRF-2016R1C1B2013642). C.W.L. was supported by the Basic Science Research Program through the National Research Foundation of Korea (NRF) funded by the Ministry of Education, Science and Technology (NRF-2016R1A2B4012593). Keping Qiu is supported by National Key R&D Program of China No. 2017YFA0402600, and acknowledges the support from National Natural Science Foundation of China (NSFC) through grants U1731237, 11473011, 11629302, and 11590781.

Software: STARLINK ([Currie et al. 2014](#); [Parsons et al. 2017](#); [Chapin et al. 2013](#)), The IDL Astronomy User's Library ([Landsman 1993](#)).

REFERENCES

Alves, F. O., Frau, P., Girart, J. M., et al. 2014, *A&A*, 569, L1

—. 2015, *A&A*, 574, C4

Andersson, B.-G., Lazarian, A., & Vaillancourt, J. E. 2015, *ARA&A*, 53, 501

André, P. 2015, *Highlights of Astronomy*, 16, 31

André, P., Di Francesco, J., Ward-Thompson, D., et al. 2014, *Protostars and Planets VI*, 27

André, P., Revéret, V., Könyves, V., et al. 2016, *A&A*, 592, A54

Arzoumanian, D., André, P., Didelon, P., et al. 2011, *A&A*, 529, L6

Bally, J., Walawender, J., Johnstone, D., Kirk, H., & Goodman, A. 2008, *The Perseus Cloud*, ed. B. Reipurth, 308

Bastien, P., Bissonnette, E., Simon, A., et al. 2011, in *Astronomical Society of the Pacific Conference Series*, Vol. 449, *Astronomical Polarimetry 2008: Science from Small to Large Telescopes*, ed. P. Bastien, N. Manset, D. P. Clemens, & N. St-Louis, 68

Buckle, J. V., Hills, R. E., Smith, H., et al. 2009, *MNRAS*, 399, 1026

Carney, M. T., Yıldız, U. A., Mottram, J. C., et al. 2016, *A&A*, 586, A44

Chandrasekhar, S., & Fermi, E. 1953, *ApJ*, 118, 113

Chapin, E. L., Berry, D. S., Gibb, A. G., et al. 2013, MNRAS, 430, 2545

Chen, M. C.-Y., Di Francesco, J., Johnstone, D., et al. 2016, ApJ, 826, 95

Ching, T.-C., Lai, S.-P., Zhang, Q., et al. 2017, ApJ, 838, 121

—. 2016, ApJ, 819, 159

Cho, J., & Yoo, H. 2016, ApJ, 821, 21

Chuss, D. T., Andersson, B.-G., Bally, J., et al. 2019, ApJ, 872, 187

Coudé, S., Bastien, P., Kirk, H., et al. 2016, MNRAS, 457, 2139

Cox, E. G., Harris, R. J., Looney, L. W., et al. 2018, ApJ, 855, 92

Crutcher, R. M., Nutter, D. J., Ward-Thompson, D., & Kirk, J. M. 2004, ApJ, 600, 279

Crutcher, R. M., Troland, T. H., Goodman, A. A., et al. 1993, ApJ, 407, 175

Cudlip, W., Furniss, I., King, K. J., & Jennings, R. E. 1982, MNRAS, 200, 1169

Currie, M. J., Berry, D. S., Jenness, T., et al. 2014, in Astronomical Data Analysis Software and Systems XXIII, Vol. 485, 391

Das, I., & Weingartner, J. C. 2016, MNRAS, 457, 1958

Davis, L. 1951, Physical Review, 81, 890

Dempsey, J. T., Friberg, P., Jenness, T., et al. 2013, MNRAS, 430, 2534

Dolginov, A. Z., & Mitrofanov, I. G. 1976, Ap&SS, 43, 291

Dotson, J. L., Vaillancourt, J. E., Kirby, L., et al. 2010, ApJS, 186, 406

Drabek, E., Hatchell, J., Friberg, P., et al. 2012, MNRAS, 426, 23

Draine, B. T., & Weingartner, J. C. 1997, ApJ, 480, 633

Evans, II, N. J., Dunham, M. M., Jørgensen, J. K., et al. 2009, ApJS, 181, 321

Fissel, L. M., Ade, P. A. R., Angilè, F. E., et al. 2016, ApJ, 824, 134

Forbrich, J., Wiesemeyer, H., Thum, C., Belloche, A., & Menten, K. M. 2008, A&A, 492, 757

Franco, G. A. P., Alves, F. O., & Girart, J. M. 2010, ApJ, 723, 146

Franzmann, E. L., & Fiege, J. D. 2017, MNRAS, 466, 4592

Friberg, P., Bastien, P., Berry, D., et al. 2016, in Proc. SPIE, Vol. 9914, Millimeter, Submillimeter, and Far-Infrared Detectors and Instrumentation for Astronomy VIII, 991403

Friberg, P., Berry, D., Savini, G., et al. 2018, in Society of Photo-Optical Instrumentation Engineers (SPIE) Conference Series, Vol. 10708, Millimeter, Submillimeter, and Far-Infrared Detectors and Instrumentation for Astronomy IX, 107083M

Friesen, R. K., Pineda, J. E., co-PIs, et al. 2017, ApJ, 843, 63

Gerin, M., Pety, J., Commerçon, B., et al. 2017, A&A, 606, A35

Girart, J. M., Rao, R., & Marrone, D. P. 2006, Science, 313, 812

Gold, T. 1952, MNRAS, 112, 215

Goldreich, P., & Kylafis, N. D. 1981, ApJL, 243, L75

—. 1982, ApJ, 253, 606

Goodman, A. A., Crutcher, R. M., Heiles, C., Myers, P. C., & Troland, T. H. 1989, ApJL, 338, L61

Gould, B. A. 1879, Resultados del Observatorio Nacional Argentino, 1

Greaves, J. S., Holland, W. S., Friberg, P., & Dent, W. R. F. 1999, ApJL, 512, L139

Greaves, J. S., Holland, W. S., Jenness, T., et al. 2003, MNRAS, 340, 353

Hatchell, J., & Dunham, M. M. 2009, A&A, 502, 139

Hildebrand, R. H. 1983, QJRAS, 24, 267

Hildebrand, R. H., Kirby, L., Dotson, J. L., Houde, M., & Vaillancourt, J. E. 2009, ApJ, 696, 567

Hiltner, W. A. 1949, ApJ, 109, 471

Hirano, N., Kamazaki, T., Mikami, H., Ohashi, N., & Umemoto, T. 1999, in Star Formation 1999, ed. T. Nakamoto, 181–182

Hirano, N., Kameya, O., Mikami, H., Umemoto, T., & Yamamoto, S. 1997, ApJ, 478, 631

Hirano, N., & Liu, F.-c. 2014, ApJ, 789, 50

Hirota, T., Honma, M., Imai, H., et al. 2011, PASJ, 63, 1

Hirota, T., Bushimata, T., Choi, Y. K., et al. 2008, PASJ, 60, 37

Ho, P. T. P., & Townes, C. H. 1983, ARA&A, 21, 239

Hoang, T., Cho, J., & Lazarian, A. 2018, ApJ, 852, 129

Hoang, T., & Lazarian, A. 2009, ApJ, 697, 1316

—. 2016, ApJ, 831, 159

Holland, W. S., Bintley, D., Chapin, E. L., et al. 2013, MNRAS, 430, 2513

Houde, M., Hull, C. L. H., Plambeck, R. L., Vaillancourt, J. E., & Hildebrand, R. H. 2016, ApJ, 820, 38

Houde, M., Rao, R., Vaillancourt, J. E., & Hildebrand, R. H. 2011, ApJ, 733, 109

Houde, M., Vaillancourt, J. E., Hildebrand, R. H., Chitsazzadeh, S., & Kirby, L. 2009, ApJ, 706, 1504

Hull, C. L. H., Plambeck, R. L., Kwon, W., et al. 2014, ApJS, 213, 13

Hull, C. L. H., Girart, J. M., Tychoniec, L., et al. 2017a, *ApJ*, 847, 92

Hull, C. L. H., Mocz, P., Burkhardt, B., et al. 2017b, *ApJL*, 842, L9

Jones, T. J., Bagley, M., Krajny, M., Andersson, B.-G., & Bastien, P. 2015, *AJ*, 149, 31

Jones, T. J., Gordon, M., Shenoy, D., et al. 2016, *AJ*, 151, 156

Jones, T. J., Klebe, D., & Dickey, J. M. 1992, *ApJ*, 389, 602

Kataoka, A., Machida, M. N., & Tomisaka, K. 2012, *ApJ*, 761, 40

Kauffmann, J., Bertoldi, F., Bourke, T. L., Evans, II, N. J., & Lee, C. W. 2008, *A&A*, 487, 993

Kirk, J. M., Ward-Thompson, D., & Crutcher, R. M. 2006, *MNRAS*, 369, 1445

Koch, E. W., & Rosolowsky, E. W. 2015, *MNRAS*, 452, 3435

Koch, P. M., Tang, Y.-W., Ho, P. T. P., et al. 2018, *ApJ*, 855, 39

—. 2014, *ApJ*, 797, 99

Krumholz, M. R. 2014, *PhR*, 539, 49

Kwon, J., Doi, Y., Tamura, M., et al. 2018, *ApJ*, 859, 4

Landsman, W. B. 1993, in *Astronomical Society of the Pacific Conference Series*, Vol. 52, *Astronomical Data Analysis Software and Systems II*, ed. R. J. Hanisch, R. J. V. Brissenden, & J. Barnes, 246

Lazarian, A. 1997, *ApJ*, 483, 296

—. 2007, *JQSRT*, 106, 225

Lazarian, A., & Hoang, T. 2007a, *MNRAS*, 378, 910

—. 2007b, *ApJL*, 669, L77

Levrier, F., Neveu, J., Falgarone, E., et al. 2018, *ArXiv e-prints*, arXiv:1802.08725

Liu, J., Qiu, K., Berry, D., et al. 2019, *arXiv e-prints*, arXiv:1902.07734

Mairs, S., Johnstone, D., Kirk, H., et al. 2015, *MNRAS*, 454, 2557

—. 2016, *MNRAS*, 461, 4022

Matthews, B. C., Hogerheijde, M. R., Jørgensen, J. K., & Bergin, E. A. 2006, *ApJ*, 652, 1374

Matthews, B. C., McPhee, C. A., Fissel, L. M., & Curran, R. L. 2009, *ApJS*, 182, 143

Matthews, B. C., & Wilson, C. D. 2002, *ApJ*, 574, 822

Maury, A. J., Girart, J. M., Zhang, Q., et al. 2018, *MNRAS*, 477, 2760

Montier, L., Plaszczynski, S., Levrier, F., et al. 2015, *A&A*, 574, A136

Naghizadeh-Khouei, J., & Clarke, D. 1993, *A&A*, 274, 968

Ordog, A., Brown, J. C., Kothes, R., & Landecker, T. L. 2017, *A&A*, 603, A15

Ortiz-León, G. N., Loinard, L., Dzib, S. A., et al. 2018, *ApJ*, 865, 73

Ostriker, E. C., Stone, J. M., & Gammie, C. F. 2001, *ApJ*, 546, 980

Padoan, P., Federrath, C., Chabrier, G., et al. 2014, *Protostars and Planets VI*, 77

Pagani, L., Steinacker, J., Bacmann, A., Stutz, A., & Henning, T. 2010, *Science*, 329, 1622

Parsons, H. A. L., Berry, D. S., Rawlings, M. G., & Graves, S. F. 2017, *Starlink Cookbook*, 22

Pattle, K., Ward-Thompson, D., Berry, D., et al. 2017, *ApJ*, 846, 122

Pezzuto, S., Elia, D., Schisano, E., et al. 2012, *A&A*, 547, A54

Planck Collaboration, Ade, P. A. R., Aghanim, N., et al. 2015a, *Astronomy & Astrophysics*, 576, A104

—. 2015b, *A&A*, 576, A105

Redaelli, E., Alves, F. O., Caselli, P., et al. 2017, *ApJ*, 850, 202

Sadavoy, S. I., Di Francesco, J., Johnstone, D., et al. 2013, *ApJ*, 767, 126

Schlafly, E. F., Green, G., Finkbeiner, D. P., et al. 2014, *ApJ*, 786, 29

Shirley, Y. L. 2015, *PASP*, 127, 299

Soam, A., Pattle, K., Ward-Thompson, D., et al. 2018, *ApJ*, 861, 65

Tang, Y.-W., Ho, P. T. P., Koch, P. M., & Rao, R. 2010, *ApJ*, 717, 1262

Tomisaka, K. 2015, *ApJ*, 807, 47

Vaillancourt, J. E., & Matthews, B. C. 2012, *ApJS*, 201, 13

Vidal, M., Leahy, J. P., & Dickinson, C. 2016, *MNRAS*, 461, 698

Wang, J.-W., Lai, S.-P., Eswaraiah, C., et al. 2018, *arXiv e-prints*, arXiv:1812.05818

Ward-Thompson, D., Pattle, K., Bastien, P., et al. 2017, *ApJ*, 842, 66

Wardle, J. F. C., & Kronberg, P. P. 1974, *ApJ*, 194, 249

Weingartner, J. C., & Draine, B. T. 2001, *ApJ*, 548, 296

—. 2003, *ApJ*, 589, 289

Zhang, Q., Qiu, K., Girart, J. M., et al. 2014, *ApJ*, 792, 116

APPENDIX

A. EFFECT OF MOLECULAR CONTAMINATION

Another effect which may influence the measured fractions of polarization is the contribution from molecular line emission at submillimeter wavelengths. The ^{12}CO $J=3-2$ molecular line in particular has been shown in some special cases to be a significant source of contamination in SCUBA-2 continuum observations at $850\text{ }\mu\text{m}$ (Drabek et al. 2012). While relatively rare, high levels of ^{12}CO $J=3-2$ line contamination (>10 per cent) in star-forming regions are usually associated with molecular outflows from young stellar objects (e.g., Chen et al. 2016; Coudé et al. 2016). This behavior occurs in SCUBA-2 observations of Perseus B1, where Sadavoy et al. (2013) found ^{12}CO $J=3-2$ line contamination levels of 90 per cent in the outflows of B1-c, 15 per cent in the central region of B1, and < 1 per cent in the rest of the cloud.

It is important to note that HARP, SCUBA-2, and POL-2 are not sensitive to the same spatial scales due to their different observing strategies. Specifically, SCUBA-2 observations for the JCMT Gould Belt Survey were taken using a PONG 1800 observing mode that is sensitive to larger spatial scales than the Daisy mode used for POL-2 (Chapin et al. 2013; Friberg et al. 2016). We therefore expect contamination levels for POL-2 to be different than those previously measured for SCUBA-2 alone, but nonetheless still confined to molecular outflows if present. Similarly, HARP observations are sensitive to larger angular scales than those from SCUBA-2, and they had to be spatially filtered during data reduction to be subtracted accurately from the $850\text{ }\mu\text{m}$ maps of the JCMT Gould Belt Survey (e.g., Mairs et al. 2016). Such a subtraction procedure for ^{12}CO $J=3-2$ molecular line contamination could potentially be adapted for future analyses of BISTRO observations.

The emission from the ^{12}CO $J=3-2$ molecular line can be weakly linearly polarized by magnetic fields through the Goldreich-Kylafis effect (Goldreich & Kylafis 1981, 1982). Observational evidence, however, suggests that this polarization is only on the order of 1 per cent for single-dish observatories (e.g., Greaves et al. 1999; Forbrich et al. 2008). Such a level of polarization would only be detectable by POL-2 in extreme cases of molecular contamination, such as the unlikely scenario of a $\sim 1.3\text{ Jy beam}^{-1}$ submillimeter source with a ^{12}CO $J=3-2$ contamination level of 90 per cent (assuming a 3σ detection threshold of $I_P \sim 12\text{ mJy beam}^{-1}$, and the maximum contamination fraction measured by Sadavoy et al. 2013). If there is significant contamination from the ^{12}CO $J=3-2$ molecular line in POL-2 observations at $850\text{ }\mu\text{m}$, it is reasonable to assume that this additional contribution to the continuum flux is unpolarised. Therefore, the effect of contamination will be to overestimate the Stokes I total intensity while the Stokes Q and U parameters remain unchanged.

In other words, molecular contamination from the ^{12}CO $J=3-2$ molecular line will lead to an underestimation of the polarization fraction P , but the polarization angle Φ will be unaffected if the instrumental polarization is properly taken into consideration. This effect is thus unlikely to influence our characterization of the magnetic and turbulent properties of Perseus B1, although it could potentially affect the polarization fraction P plotted in Figure 2 (top). Such possible contamination may need to be taken into account for future, more detailed analysis of grain alignment efficiency using POL-2 data.

Finally, it is important to note that the Goldreich-Kylafis effect might nonetheless be important for polarimetric observations using interferometers such as the SMA. Indeed, Ching et al. (2016) measured polarization fractions up to 20 % for the ^{12}CO $J=3-2$ emission towards the IRAS 4A protostellar outflow. In such cases, continuum measurements of the Stokes Q and U parameters are likely to be affected by strong ^{12}CO line contamination of the Stokes I total intensity.